

Cross-Species Single-Cell Analysis of Pancreatic Ductal Adenocarcinoma Reveals Antigen-Presenting Cancer-Associated Fibroblasts

Ela Elyada^{1,2}, Mohan Bolisetty^{3,4}, Pasquale Laise⁵, William F. Flynn³, Elise T. Courtois³, Richard A. Burkhardt⁶, Jonathan A. Teinor⁶, Pascal Belleau¹, Giulia Biffi^{1,2}, Matthew S. Lucito^{1,2}, Santhosh Sivajothi³, Todd D. Armstrong⁶, Dannielle D. Engle^{1,2,7}, Kenneth H. Yu⁸, Yuan Hao¹, Christopher L. Wolfgang⁶, Youngkyu Park^{1,2}, Jonathan Preall¹, Elizabeth M. Jaffee⁶, Andrea Califano^{5,9,10,11,12}, Paul Robson^{3,13}, and David A. Tuveson^{1,2}

ABSTRACT

Cancer-associated fibroblasts (CAF) are major players in the progression and drug resistance of pancreatic ductal adenocarcinoma (PDAC). CAFs constitute a diverse cell population consisting of several recently described subtypes, although the extent of CAF heterogeneity has remained undefined. Here we use single-cell RNA sequencing to thoroughly characterize the neoplastic and tumor microenvironment content of human and mouse PDAC tumors. We corroborate the presence of myofibroblastic CAFs and inflammatory CAFs and define their unique gene signatures *in vivo*. Moreover, we describe a new population of CAFs that express MHC class II and CD74, but do not express classic costimulatory molecules. We term this cell population “antigen-presenting CAFs” and find that they activate CD4⁺ T cells in an antigen-specific fashion in a model system, confirming their putative immune-modulatory capacity. Our cross-species analysis paves the way for investigating distinct functions of CAF subtypes in PDAC immunity and progression.

SIGNIFICANCE: Appreciating the full spectrum of fibroblast heterogeneity in pancreatic ductal adenocarcinoma is crucial to developing therapies that specifically target tumor-promoting CAFs. This work identifies MHC class II-expressing CAFs with a capacity to present antigens to CD4⁺ T cells, and potentially to modulate the immune response in pancreatic tumors.

See related commentary by Belle and DeNardo, p. 1001.

¹Cold Spring Harbor Laboratory, Cold Spring Harbor, New York. ²Lustgarten Foundation Pancreatic Cancer Research Laboratory, Cold Spring Harbor, New York. ³The Jackson Laboratory for Genomic Medicine, Farmington, Connecticut. ⁴Bristol-Myers Squibb, Pennington, New Jersey. ⁵Department of Systems Biology, Columbia University Irving Medical Center, New York, New York. ⁶Sidney Kimmel Comprehensive Cancer Center, Johns Hopkins University, Baltimore, Maryland. ⁷Salk Institute for Biological Studies, La Jolla, California. ⁸Memorial Sloan Kettering Cancer Center, New York, New York. ⁹Herbert Irving Comprehensive Cancer Center, Columbia University, New York, New York. ¹⁰J.P. Sulzberger Columbia Genome Center, Columbia University, New York, New York. ¹¹Department of Biomedical Informatics, Columbia University, New York, New York. ¹²Department of Biochemistry and Molecular Biophysics, Columbia University, New York, New York. ¹³Department of Genetics and Genome Sciences, Institute for Systems Genomics, University of Connecticut, Farmington, Connecticut.

Note: Supplementary data for this article are available at Cancer Discovery Online (<http://cancerdiscovery.aacrjournals.org/>).

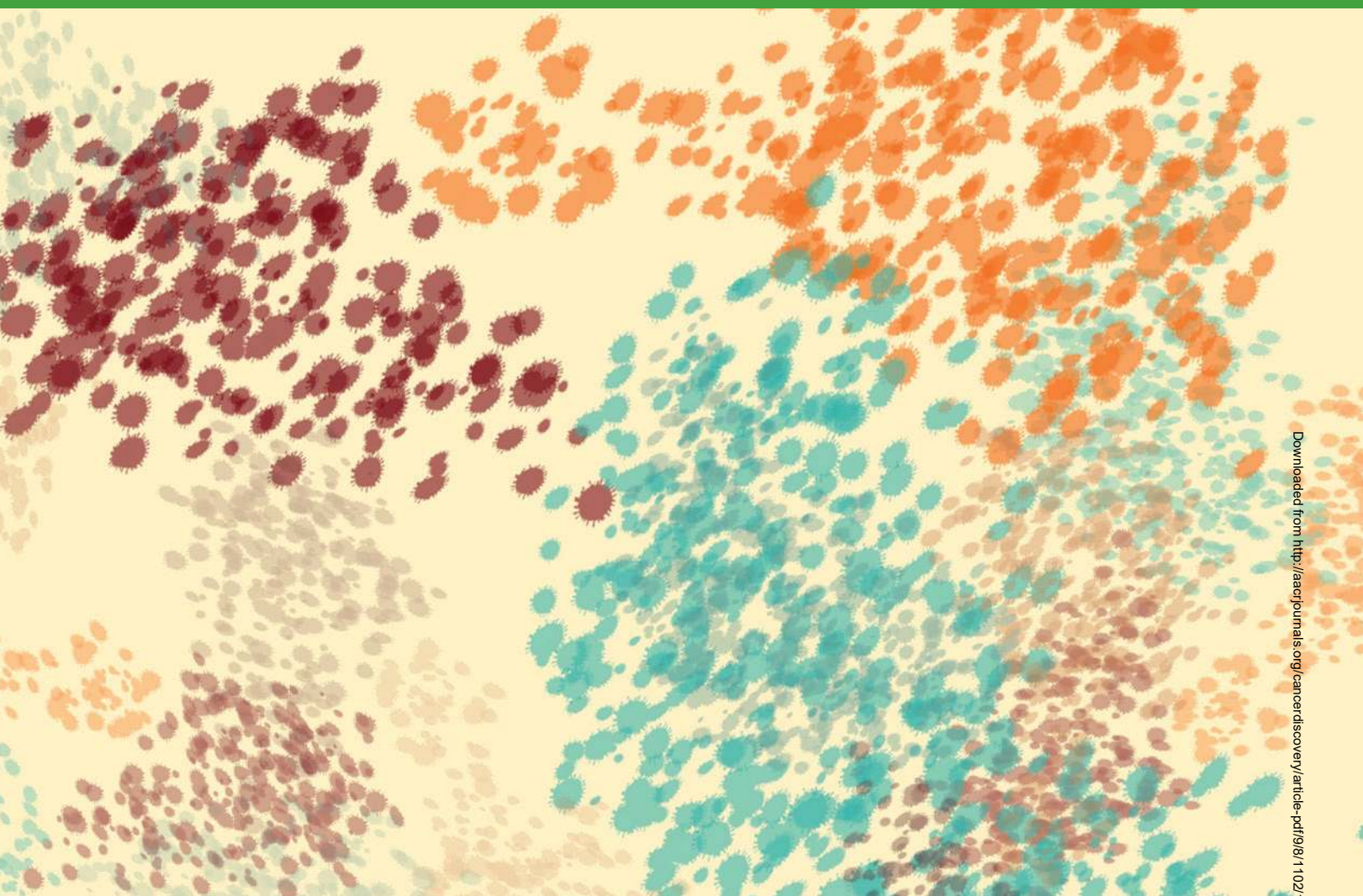
M. Bolisetty, P. Laise, and W.F. Flynn contributed equally to this article.

Corresponding Authors: David A. Tuveson, Cold Spring Harbor Laboratory, 1 Bungtown Road, Cold Spring Harbor, NY 11724. Phone: 516-367-5246; Fax: 516-367-8353; E-mail: dtuveson@csh.edu; and Paul Robson, The Jackson Laboratory, 10 Discovery Drive, Farmington, CT 06032. Phone: 207-288-6594; Fax: 860-837-2398; E-mail: paul.robson@jax.org

Cancer Discov 2019;9:1102–23

doi: 10.1158/2159-8290.CD-19-0094

©2019 American Association for Cancer Research.



INTRODUCTION

Pancreatic ductal adenocarcinoma (PDAC) is a deadly disease that thus far has no effective treatment (1). PDAC is characterized by an abundance of nonmalignant stromal cells that support the proliferation, survival, and invasion of cancer cells (2). Among these stromal cells, cancer-associated fibroblasts (CAF) play a major role in facilitating tumor growth (3). CAFs produce components of the extracellular matrix (ECM), which has been shown to provide survival and migration cues to cancer cells (4, 5) and to physically interfere with drug delivery in PDAC mouse models (6–8). CAFs mediate collagen cross-linking in the extracellular space, thereby modulating tumor stiffness and facilitating cancer progression (9–11). CAFs also secrete multiple cytokines, chemokines, and growth factors, which support cancer cells both directly and indirectly (3). Although these CAF-derived factors serve as direct survival signals to cancer cells, they also alter the immune cell milieu by inhibiting the activity of immune-effector cells and recruiting immune-suppressive cells, allowing cancer cells to evade immune surveillance (12–18).

Given the evidence suggesting that CAFs play a tumor-supportive role, therapeutic strategies to deplete fibroblasts should be an effective strategy to target PDAC. However, the dogma that CAFs are solely tumor-promoting has been challenged in recent years by studies aiming to target stromal fibroblasts. For instance, although ablation of cells that express the myofibroblast marker alpha smooth muscle actin (α SMA) in a PDAC mouse model reduced desmoplasia, the resulting tumors were highly undifferentiated, intratumoral blood vessels were further diminished in number with hypoxic necrosis evident, and the animal survival was shortened (19). Additionally, chronic treatment with a Smoothed inhibitor or neoplastic cell deletion of Sonic Hedgehog 1, a major mediator of desmoplasia, in a PDAC mouse model resulted in a similar phenotype (20, 21). These studies suggest that some CAFs function to restrain tumor growth rather than accelerate it. The use of a Hedgehog pathway reporter allele revealed that nearly all α SMA-expressing fibroblasts are hedgehog-responsive, linking myofibroblasts with the tumor-restraining Hedgehog pathway (20). Further supporting this notion, a clinical trial that combined chemotherapy with

IPI-926, a small-molecule inhibitor of the Hedgehog pathway, failed to show benefit and was aborted due to a shortened patient overall survival (NCT01130142; refs. 22, 23). This suggests that the Hedgehog-responsive fibroblasts attenuate tumor progression and the pathophysiology of PDAC *in vivo*.

One way to reconcile these contrasting observations is to abandon the original notion of CAFs as a uniform population of cells in favor of a new model where the tumor microenvironment comprises a heterogeneous population of CAFs with different functions within PDAC tumors. In support of this idea, we previously demonstrated the coexistence of two distinct subtypes of CAFs in PDAC: CAFs expressing high levels of α SMA, which we therefore named “myfibroblastic CAFs” (myCAF), and CAFs expressing low levels of α SMA but high levels of cytokines and chemokines, which we named “inflammatory CAFs” (iCAF; ref. 16). These two CAF subtypes were found in disparate locations relative to the cancer cells: Whereas myCAFs were primarily adjacent to cancer cells, iCAFs were located in the desmoplastic areas of the tumor, farther away from the cancer cells (16). Although our results demonstrate the existence of more than one CAF population in the PDAC microenvironment, the full complement of CAF populations remains unclear. To address this question, we sought to investigate the heterogeneity of CAFs in PDAC at single-cell resolution.

Here, we applied single-cell RNA sequencing (RNA-seq) to PDAC tumor tissue from six human patients, adjacent-normal pancreas tissue from two of these patients, and PDAC tumors from four *Kras*^{+/LSL-G12D}; *Trp53*^{+/LSL-R172H}; *Pdx1-Cre* (KPC) mice. This method identified various subpopulations known to be present in PDAC tumors, including ductal epithelial cells and a variety of myeloid and lymphoid cells, as well as different subsets of fibroblasts. We further confirmed the existence of distinct myCAF and iCAF subpopulations and defined gene signatures that characterize these populations *in vivo*. Interestingly, we also identified a new CAF subtype that expresses MHC class II (MHCII)-related genes and induces T-cell receptor (TCR) ligation in CD4⁺ T cells in an antigen-dependent manner. We therefore named these cells “antigen-presenting CAFs” (apCAF). We demonstrated that apCAFs can convert into myfibroblasts upon suitable culture conditions, suggesting that pancreatic CAF subpopulations represent dynamic and interconvertible states.

RESULTS

Single-Cell Analysis Uncovers the Complexity of Human PDAC

To comprehensively catalog the populations of cells that are present in human PDAC, we undertook a single-cell RNA-seq approach to transcriptionally characterize a large number of cells from primary tumors. Six tumors from patients with untreated PDAC and adjacent-normal pancreas tissues from two of these patients (Supplementary Table S1) were enzymatically digested to generate single-cell suspensions (Supplementary Table S2). Fluorescence-activated cell sorting (FACS) was used to isolate viable cells via DAPI staining, and to enrich for fibroblasts by negative selection of non-fibroblast populations (Fig. 1A). Single cells from each sample were captured and sequenced using a droplet-based

approach (24). To increase our analytic power, data from the viable cell fraction of all tumor and adjacent-normal samples were combined into a single set for a total of 21,200 cells (Supplementary Fig. S1A–S1D). Highly variable genes were identified from the combined data set, and these were used to embed the data set in two dimensions using t-distributed stochastic neighbor embedding (t-SNE). Density-based clustering (25) was used to identify 15 distinct clusters, with an average of 5,246 transcripts and 1,576 genes per cluster (Fig. 1B; Supplementary Fig. S1E and S1F; Supplementary Table S3). Signature genes within each cluster were cross-referenced with known markers of cell populations from the literature to identify the different cell types that are represented by the clusters (Fig. 1C; Supplementary Table S4).

Within the viable cell fraction, the majority of cells in our analysis (89%) were classified as immune cells, including various cell types of the myeloid and lymphoid lineages (Fig. 1B; Supplementary Table S4). This bias toward immune cells in our cell suspension suggests that immune cells are readily detached from PDAC tissues. In contrast, fibroblasts comprised only 1.75% of the cells sorted, reflecting the challenge in releasing this population in a viable state from the tumor (Fig. 1B, cluster 7). We also detected the glandular components of the pancreas—acinar cells (Fig. 1B, cluster 6) and ductal cells, for which three distinct clusters were identified (Fig. 1B; Supplementary Table S3, clusters 2, 8, and 15). The profiles of cell clusters seen in each specimen were heterogeneous (Supplementary Fig. S1G and S1H); however, as a group, tumor and adjacent-normal tissues both contributed to all cell clusters (Supplementary Fig. S1I and S1J). Notably, the fibroblast cluster was derived mostly from tumor samples, in line with the rich fibrosis that is a hallmark of PDAC (Supplementary Fig. S1J, cluster 7).

Ductal Cell Subpopulations Are Present in Human PDAC

Recently, several studies have defined distinct subtypes of PDAC tumors based on bulk transcriptome analyses (26–28). To better characterize the ductal cell populations in PDAC tumors, we isolated cells from the three ductal clusters and performed a separate clustering analysis to allow for subtle differences to be detected. We identified four distinct subclusters of ductal cells (Fig. 1D), three of which were derived from both tumor and adjacent-normal samples, whereas one (subcluster 2) was derived solely from one adjacent-normal sample (Fig. 1D and E; Supplementary Fig. S1K; Supplementary Table S5). We compared marker genes of the ductal cell subclusters to the classic and basal-like gene signatures previously described in PDAC (26). We found genes belonging to the classic gene signature (*TFE1*, *TFE2*, *LYZ*, *VSIG2*, and *CEACAM6*) expressed specifically in subclusters 1 and 4 (Fig. 1F; Supplementary Table S6), whereas most basal-like genes were not detected in our ductal cells (data not shown). Subcluster 4 also had a unique signature that distinguished it from subcluster 1 (Fig. 1F; Supplementary Table S6). Subcluster 2 was derived solely from an adjacent-normal sample, expressing genes involved in lipid metabolism and processing (e.g., *APOA1*, *FABP1*, and *ADIRF*). Subcluster 3 expressed, among others, genes encoding many secreted proteins

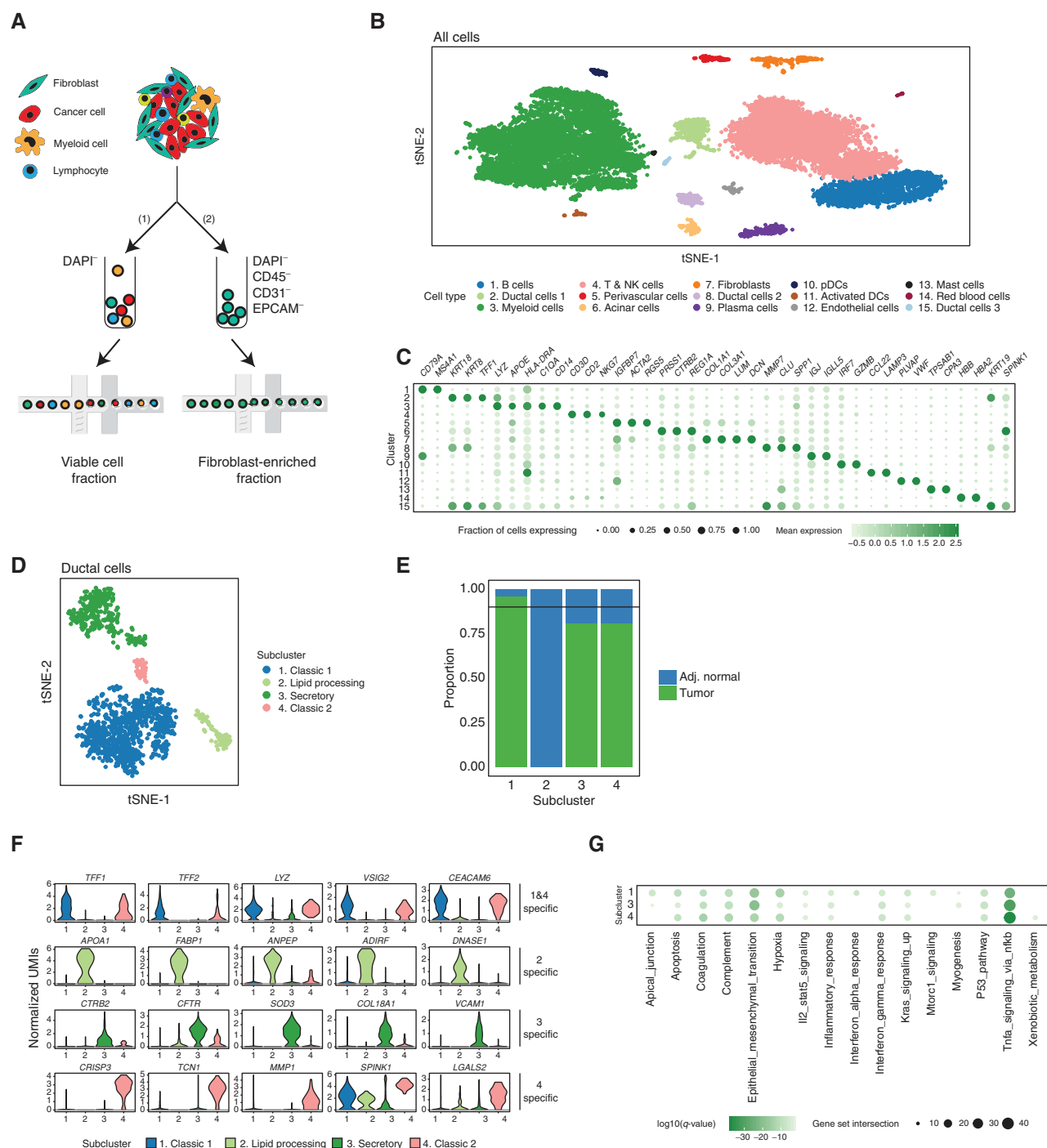


Figure 1. Single-cell analysis uncovers ductal cell subpopulations in human PDAC. **A**, Graphical scheme describing the workflow. Human and murine pancreatic tumors were dissociated into single cells. Two fractions of cells were collected by FACS from each sample: (1) all viable cell fraction (DAPI⁻); (2) fibroblast-enriched fraction (DAPI⁻, CD45⁻, CD31⁻, and EPCAM⁻). The sorted cells from each fraction were subjected to single-cell capture, barcoding, and reverse transcription using the 10X Genomics platform. **B**, Unsupervised clustering of viable cells from six human PDAC resections and two adjacent-normal pancreata, represented as a t-SNE plot. Different cell type clusters are color coded. **C**, Bubble plot showing selected cell type-specific markers across all clusters. Size of dots represents the fraction of cells expressing a particular marker, and intensity of color indicates the level of mean expression. Legends are shown below. **D**, Reclustering of the ductal cell types in the data set (clusters 2, 8, and 15 from **B**), represented as a t-SNE plot. **E**, Proportion of cells from adjacent-normal pancreata and tumor resections present in each ductal cell subcluster. The horizontal black line represents the input contribution of adjacent-normal or tumor tissues into the data set. **F**, Violin plot showing normalized expression of marker genes for the different ductal cell subclusters. UMI, unique molecular identifier. **G**, Hallmark pathways enriched in the three tumor-derived ductal cell subclusters (subclusters 1, 3, and 4) relative to the adjacent-normal-derived ductal cell subcluster (subcluster 2). The horizontal black line represents the intersection of upregulated genes (>2 logFC) with hallmark pathway gene sets, and intensity of color indicates log₁₀(q-value). Legends are shown below.

(e.g., *SPP1*, *CLU*, *MMP7*, *CTGF*, and *COL18A1*) and acinar proteins (e.g., *CTRB2* and *CFTR*; Fig. 1F; Supplementary Table S6). Interpatient heterogeneity was detected in the ductal subclusters, with almost all patients represented in subclusters 1 and 3, but only a minority in subclusters 2 and 4 (Supplementary Fig. S1K). Pathway analysis comparing the three tumor-derived clusters to subcluster 2 (adjacent-normal derived) found known PDAC driver pathways, such as the KRAS, p53, and hypoxia pathways, enriched in all three tumor-derived clusters, supporting their tumor origin (Fig. 1G). Inflammation-related pathways such as IFN γ , TNF α , IL2/STAT5, and the complement pathway were also prominent in all of the tumor-derived subclusters, likely reflecting the inflammatory nature of PDAC (Fig. 1G).

An Immune-Suppressive Environment Is Predominant in Human PDAC

In order to identify immune cell subpopulations within the myeloid and lymphoid lineages, we analyzed the two major immune cell clusters detected in human PDAC as two separate data sets, excluding all other cell types. Unsupervised dimensionality reduction and clustering were generated from all the cells belonging to cluster 3 (myeloid cells) or cluster 4 [T and natural killer (NK) cells], independently. We also separated adjacent-normal-derived cells from tumor-derived cells to assess the nature of the immune-cell populations in PDAC.

Analysis of the myeloid cluster revealed six distinct subclusters in tumor samples and four subclusters in adjacent-normal samples (Fig. 2A; Supplementary Fig. S2A and S2B; Supplementary Table S7). More than 96% of the cells in this cluster were identified as monocytes and macrophages (subclusters 1, 2, and 4), whereas a minority of the cells (<4%) were identified as dendritic cells (DC; subclusters 3, 5, and 6). Subcluster 4 was derived entirely from tumor samples (Fig. 2B; Supplementary Fig. S2B) and was annotated as alternatively activated macrophages due to high expression of *SPP1*, *LY6E*, and the macrophage scavenger receptor *MARCO* (Fig. 2C; Supplementary Table S8). Both *MARCO* and *SPP1* have been associated with a noninflammatory, immune-suppressive phenotype of macrophage activation (29–32). Expression of neutrophil markers (*S100A8*, *S100A9*, and *G0S2*) was detected in the monocyte and macrophage subclusters, indicating further heterogeneity within these myeloid subpopulations (Fig. 2D). Two of the DC subclusters (subclusters 3 and 6) expressed *CD1A* and *CD207* and were therefore identified as “Langerhans-like” DCs (Fig. 2C; Supplementary Table S8). Subcluster 5 was identified as type 1 conventional DCs (cDC1) due to expression of *CLEC9A*, *BATF3*, and *IRF8* (Fig. 2C; Supplementary Table S8). cDCs were previously reported to cross-present antigens to CD8⁺ T cells, and their presence is correlated with response to checkpoint inhibitors in patients (33, 34). However, the tumor microenvironment has been shown to educate cDCs toward a regulatory DC phenotype with immunosuppressive functions (35, 36). Accordingly, the cDCs in our data set strongly expressed *IDO1* (Fig. 2C), which catalyzes tryptophan depletion and kynurenine production, both of which inhibit T-cell proliferation and cytotoxicity (37).

The analysis of the T and NK cell cluster resulted in five distinct subclusters (Fig. 2E; Supplementary Fig. S2C; Supplementary Tables S9–S10). CD4⁺ T cells (subcluster 2) and regulatory T cells (Treg) in particular (subclusters 3 and 5) were derived almost exclusively from the tumor samples (Fig. 2F; Supplementary Fig. S2D). This is in line with the previously reported accumulation of immune-suppressive CD4⁺ T cells upon mutant KRAS activation in a PDAC mouse model (38). Tregs expressed their typical gene signature, which included immune-inhibitory molecules such as *CTLA4* and *TIGIT* (Fig. 2G; Supplementary Table S10). The role of Tregs in inhibiting immune responses in cancer has long been established (39, 40), and mechanisms of Treg infiltration have been described in PDAC as well (41–43). Our data support the accumulation of Tregs during tumorigenesis. The CD8⁺ T-cell population (subcluster 1) was characterized by low expression of activation markers for cytotoxicity such as granzyme B (*GZMB*), perforin (*PRF1*), and IFN γ (*IFNG*; Fig. 2G). However, we could detect higher expression of *IFNG* in a subset of CD8⁺ T cells that was exclusively derived from tumor samples, compared with lower expression in the subset of cells that was shared between tumor and adjacent-normal pancreas (Fig. 2H, top subcluster 1). Concomitant with the expression of *IFNG*, these cells also expressed exhaustion markers such as *LAG3* and *EOMES*, suggesting that tumor-derived T cells had become exhausted after an initial activation phase. In contrast to CD8⁺ T cells, most of the NK cells (subcluster 4, marked by *NKG7* expression) remained activated and strongly expressed *GZMB*, *PRF1*, and *IFNG* (Fig. 2G and H). Within the NK-cell subcluster, we detected a group of T cells that share properties with NK cells, which are termed “NKT cells” (Fig. 2H, bottom subcluster 4, asterisk). Cells in this subset expressed T cell-specific markers such as *CD3D* and *CD8A*, in contrast to NK cells which did not (Fig. 2H, top subcluster 4). Altogether, our single-cell analysis of the immune cells present in PDAC tumors depicts a strong immune-suppressive microenvironment, consisting of several cell types known to mediate T-cell inactivation in PDAC.

Distinct Subtypes of Cancer-Associated Fibroblasts Are Detected in Human PDAC

With the goal of unraveling the full spectrum of CAF heterogeneity in PDAC, we next sought to use our single-cell analysis of human PDAC to corroborate our previous finding of myCAF and iCAF subpopulations in the PDAC microenvironment (16). To enrich for fibroblasts, antibodies directed against CD45, CD31, and EPCAM were used to deplete immune, endothelial, and epithelial cells, respectively (Fig. 1A). Using this approach, we were able to isolate a fibroblast-enriched fraction from sample hT137 (hT137 FE). These cells were combined with the fibroblasts digitally extracted from the viable cell fraction of all other tumors, and all of these cells were analyzed together (Supplementary Table S11). A total of 962 fibroblasts were analyzed, which formed two distinct subclusters with unique gene signatures upon t-SNE analysis (Fig. 3A and B; Supplementary Table S12). Common fibroblast markers such as *COL1A1*, *FAP*, and the mesenchymal cell marker *VIM* were expressed in both CAF subpopulations, confirming their fibroblast

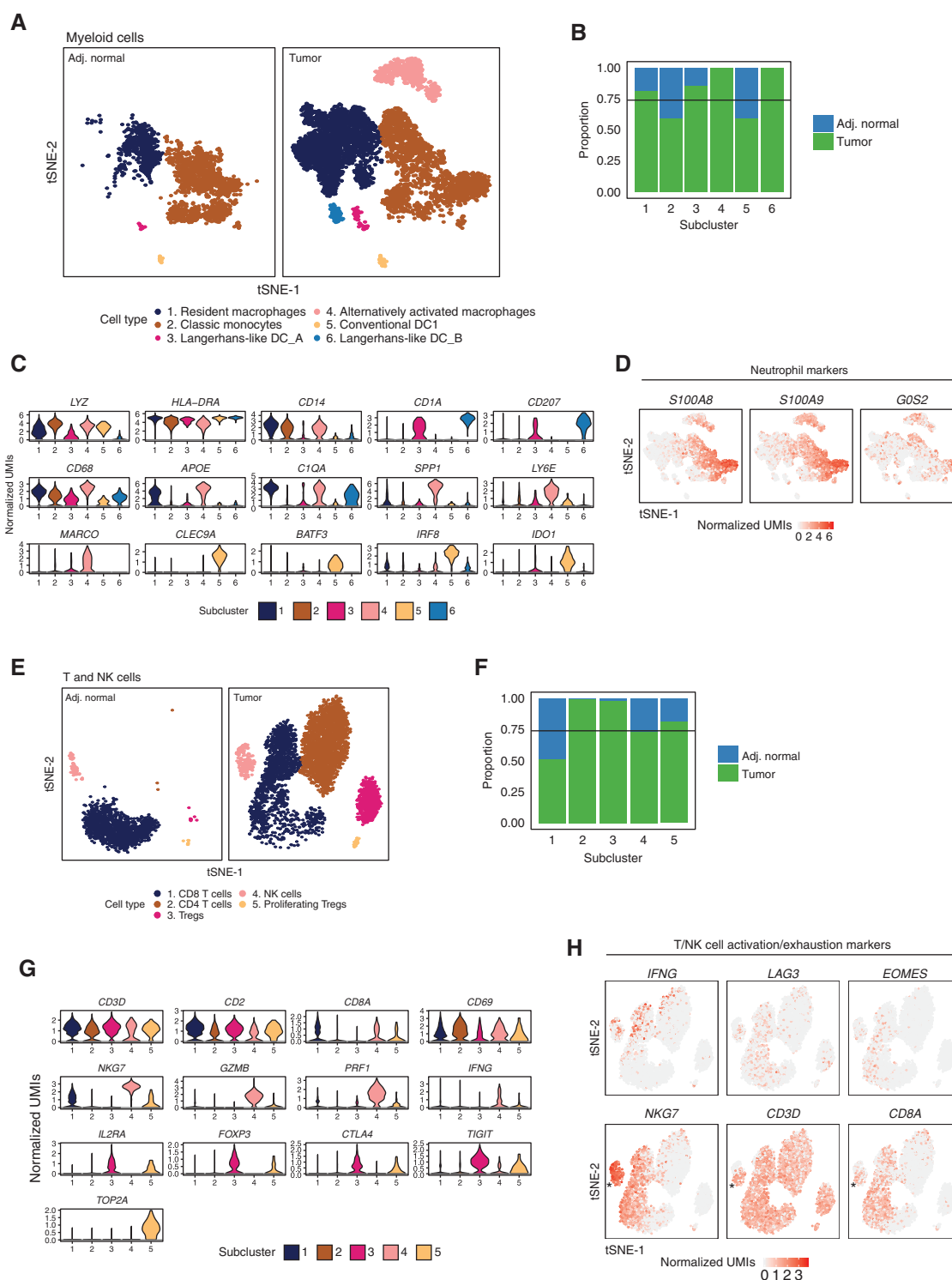
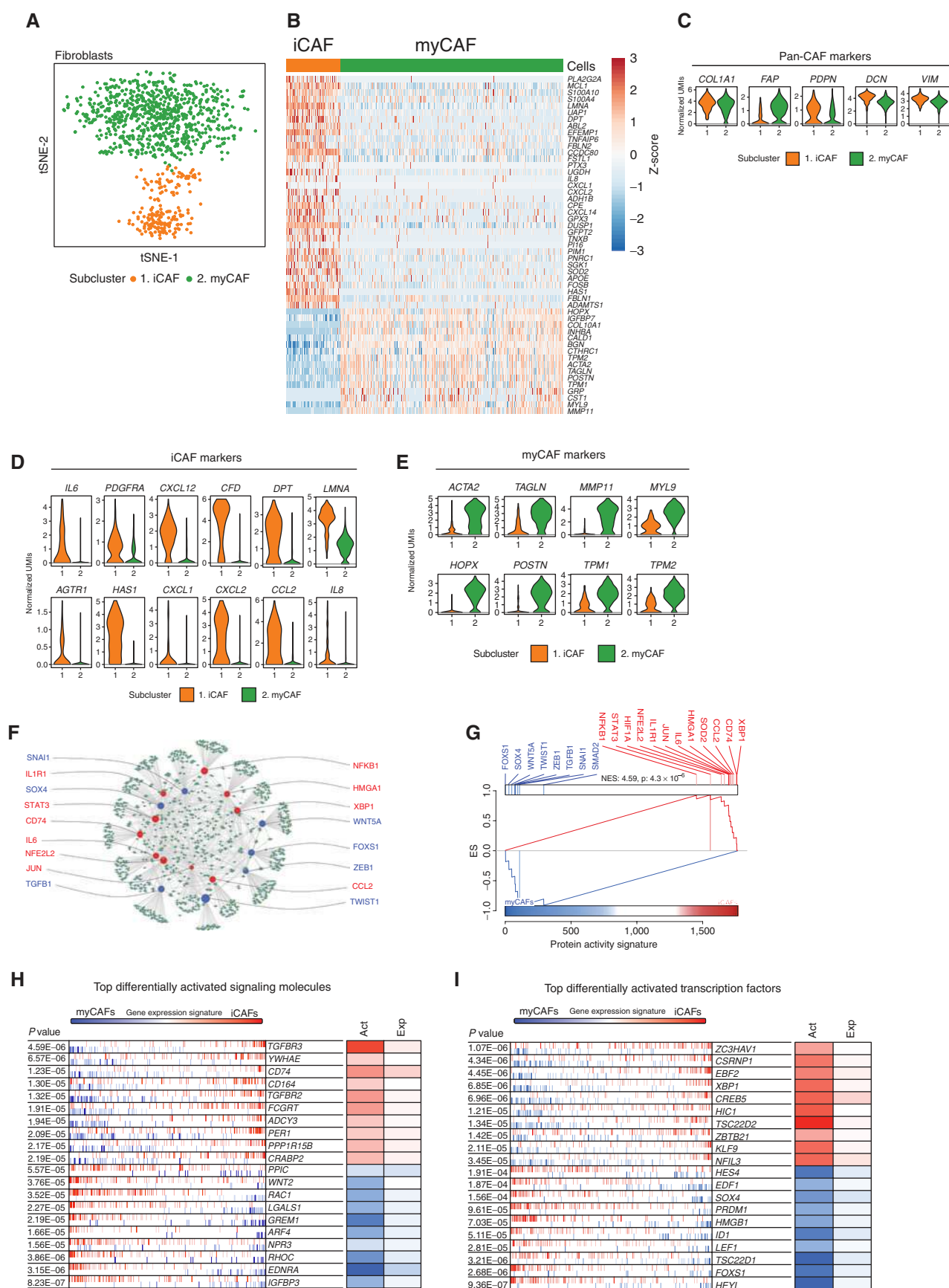


Figure 2. Immune-suppressive environment dominates human PDAC. **A**, Reclustering of the myeloid cells in the human data set (cluster 3 from Fig. 1B) represented as a t-SNE plot. **B**, Proportion of cells from adjacent-normal pancreata and tumor resections present in each myeloid cell subcluster. The horizontal black line represents the input contribution of adjacent-normal or tumor tissues into the data set. **C**, Violin plots of selected genes, showing normalized expression in the different subclusters. **D**, t-SNE plots showing expression of selected neutrophil marker genes in the myeloid subclusters. Legend shows a color gradient of normalized expression. **E**, Reclustering of the T and NK cells in the human data set (cluster 4 from Fig. 1B) represented as a t-SNE plot. **F**, Proportion of cells from adjacent-normal pancreata and tumor resections present in each lymphoid cell subcluster. The horizontal black line represents the input contribution of adjacent-normal or tumor tissues into the data set. **G**, Violin plots of selected genes, showing normalized expression in the different subclusters. **H**, t-SNE plots showing expression of selected T/NK cell activation and exhaustion marker genes in the lymphoid subclusters. Legend shows a color gradient of normalized expression. Asterisk (*) marks NKT cells within the NK cell cluster.



identity (Fig. 3C). Furthermore, we identified other common CAF markers that were expressed in both subclusters but have not been widely used as CAF markers, such as *PDPN* and *DCN* (Fig. 3C). *PDPN* has been shown to be expressed in a specific subtype of CAFs in patients with colorectal cancer (44), and high *PDPN* expression in stromal fibroblasts was correlated with poorer prognosis in patients with pancreatic cancer (45). *DCN* has been shown to be produced by fibroblasts in nonmalignant diseases (46).

In accordance with our previous iCAF and myCAF characterization (16), subcluster 1 had enriched expression of *IL6*, *IL8*, and chemokines such as *CXCL1*, *CXCL2*, *CCL2*, and *CXCL12*, and was therefore identified as iCAFs (Fig. 3D, orange; Supplementary Table S13). Subcluster 2 was identified as myCAFs because it expressed high levels of α SMA (encoded by *ACTA2*; Fig. 3E, green; Supplementary Table S13). The majority of the cells in both tumor-derived and adjacent-normal-derived samples were classified as myCAFs (Supplementary Fig. S2E and S2F; Supplementary Table S12). Although *PDGFRA* is commonly used as a CAF marker in different settings, we found that it is predominantly expressed in iCAFs (Fig. 3D). Our analysis enabled the identification of new marker genes for each CAF subtype. Strong expression of *CFD* and matrix proteins such as *LMNA* and *DPT* marked iCAFs (Fig. 3B and D; Supplementary Table S13). In contrast, myCAF markers included the contractile proteins *TAGLN*, *MYL9*, *TPM1*, *TPM2*, *MMP11*, *POSTN*, and *HOPX* (Fig. 3B and E; Supplementary Table S13). Notably, specific to iCAFs was expression of *HAS1* and *HAS2*, the enzymes responsible for the synthesis of hyaluronan, a major component of the ECM identified as a significant barrier to treatment of PDAC (Fig. 3D; Supplementary Table S13; refs. 7, 47). In addition, iCAFs differentially expressed *AGTR1* (encoding AT1; Fig. 3D), which is a subject for targeted inhibition in ongoing clinical trials in patients with PDAC (NCT01821729 and NCT03563248; ref. 48). Using gene set enrichment analysis (GSEA), we identified pathways enriched among the differentially expressed genes in myCAFs and iCAFs. Smooth muscle contraction, focal adhesion, ECM organization, and collagen formation were significantly upregulated in myCAFs (Supplementary Fig. S3A; Supplementary Table S14), whereas inflammatory pathways such as IFN γ response, TNF/NF- κ B, IL2/STAT5, IL6/JAK/STAT3, and the complement pathway were upregulated in iCAFs (Supplementary Fig. S3B; Supplementary Table S14). These results are in concordance with pathways that we previ-

ously identified to be differentially expressed in bulk and single-cell RNA-seq of mouse CAF subsets *in vitro* and *in vivo* (16, 49).

We have recently determined that IL1/JAK-STAT3 and TGF β /SMAD2/3 are two opposing pathways that induce either iCAF or myCAF formation, respectively (49). To confirm these pathways are active in our two CAF subpopulations, and to identify novel regulatory proteins that are differentially activated between human iCAFs and myCAFs, we applied the virtual inference of protein activity by enriched regulon analysis (VIPER) algorithm (50). This algorithm uses the expression of the target genes regulated by a given protein (referred to as a regulon) as a reporter for that protein's activity. We first used the algorithm for the reconstruction of accurate cellular networks (ARACNe; ref. 51) to infer the regulons associated with transcription factors and signaling molecules in iCAFs and myCAFs. We then applied VIPER to identify the differentially activated regulators between the two CAF subtypes. In line with our recent observation on the determinants of iCAF and myCAF phenotypes (49), we found IL1R1 and STAT3 to be differentially activated in iCAFs, whereas TGF β 1 and SMAD2 were activated in myCAFs (Fig. 3F and G; Supplementary Tables S15–S16). Surprisingly, among the top differentially activated proteins in iCAFs compared with myCAFs were the TGF β receptors TGFBR2 and TGFBR3 (Fig. 3H; Supplementary Table S15). The presence of active TGF β receptors in iCAFs, which do not show an activated TGF β program, may indicate a negative feedback loop arising from the absence of TGF β signaling in these cells. As expected, chemokine and cytokine networks (e.g., IL6 and CCL2) were active in iCAFs, concomitant with activation of the NF- κ B pathway, which is known to regulate many inflammatory cytokines (Fig. 3F and G; Supplementary Tables S15–S16). Other transcription factors (EBF2 and XBP1) and receptors (CD74 and FCGRT) known to regulate immune response were among the top 10 most active regulators in iCAFs, supporting the notion that the iCAF cluster contains immune-modulating cells (Fig. 3H and I). In addition, the hypoxia regulator HIF1 α and the redox regulators NRF2 (NFE2L2) and SOD2 were active in iCAFs, suggesting a role for iCAFs in oxidative stress relief (Fig. 3F and G; Supplementary Tables S15–S16). Lastly, *AGTR1* is also active in the iCAF compartment (Supplementary Tables S16). In contrast, transcription factors known to promote a mesenchymal cell state (e.g., TWIST1, ZEB1, SNAI1, and SOX4) were active in myCAFs (Fig. 3F and G; Supplementary Table S15).

Figure 3. Distinct subtypes of CAFs are detected in human PDAC. **A**, Reclustering of CAFs in the human data set (cluster 7 from Fig. 1B) represented as a t-SNE plot. **B**, Heat map showing scaled normalized expression of discriminative marker genes between the two subclusters, with cells as columns and genes as rows. Color scheme represents Z-score distribution from -3 (blue) to 3 (dark orange). **C–E**, Violin plot of selected pan-CAF markers (**C**), iCAF markers (**D**), and myCAF markers (**E**) showing normalized expression in each of the subclusters. **F**, Network representation of selected differentially activated proteins between human iCAFs and myCAFs, as analyzed by VIPER. Proteins activated in iCAFs are shown in red; proteins activated in myCAFs are shown in blue. **G**, GSEA plot showing the enrichment score (ES) for a selected set of differentially activated proteins in iCAFs (shown in red) and myCAFs (shown in blue). **H–I**, VIPER plot showing the enrichment for the top 20 differentially activated signaling molecules (**H**) or transcription factors (**I**) between iCAFs and myCAFs. The top bar represents the ranked gene-expression signature between myCAFs and iCAFs. Regulatory target genes in each signaling molecule regulon or transcription factor regulon are represented by vertical lines projected along the gene-expression signature. Each vertical line represents the position of a regulatory target gene in the ranked signature between myCAFs and iCAFs. The colors of the lines indicate if the regulatory targets are positively (red) or negatively (blue) regulated by their corresponding signaling molecule or transcription factor, according to the ARACNe/VIPER inferred regulatory model. The two-column heat map on the right shows the inferred differential activity (Act) and the differential gene expression (Exp) of each regulon. The column on the left shows the P values associated with the enrichment of each regulon.

These are known target genes of the TGF β pathway, consistent with our detection of TGF β activity in these cells. Additionally, noncanonical WNT signaling molecules (WNT2 and WNT5A), which are implicated in myocyte differentiation and fibrosis (52, 53), were differentially active in myCAFs (Fig. 3F–I; Supplementary Tables S15–S16). Our protein-activity analysis identifies new regulators of human CAFs and provides another level of divergence between the two CAF subpopulations. Altogether, our results lend further support to the existence of two functionally distinct CAF populations in human PDAC tumors.

Single-Cell Analysis of KPC Tumors Recapitulates Human PDAC

Although our results in human PDAC specimens confirmed the presence of iCAFs and myCAFs, this analysis was restricted to a relatively modest number of fibroblasts. To allow deeper CAF characterization, we extended our investigation to the KPC mouse model of PDAC (54). Pancreatic tumors from four KPC mice were dissociated into single cells. From each tumor we isolated two fractions of cells by FACS: (i) a viable cell population and (ii) a fibroblast-enriched population (Fig. 1A). Sorted cells were subjected to the same droplet-based protocol for single-cell capture and library preparation. The sequencing data from the viable cell populations isolated from the four KPC tumors were merged into one data set containing a total of 11,260 viable cells, with a median of 5,989 unique transcripts and 1,916 unique genes per cell (Fig. 4A; Supplementary Fig. S4A–S4D; Supplementary Table S17). Clustering analysis of this data set resulted in 12 clusters, with a median of 6,720 transcripts and 2,048 genes per cluster (Fig. 4A and B; Supplementary Fig. S4E–S4F; Supplementary Table S17). Cell-type determination was performed using marker genes curated from the literature (Fig. 4A and B; Supplementary Table S18). Similar to human PDAC, KPC tumors contained a preponderance (~87%) of myeloid cells, consisting of mostly macrophages and neutrophils, with a small subset of DCs (Fig. 4A and B). However, mouse PDAC was distinct in its substantially lower fraction of B and T lymphocytes, in agreement with reports showing exclusion of T cells from pancreatic tumors in mouse models (17, 55). The fraction of fibroblasts in the KPC tumors was similar to that of human PDAC samples (2% of all cells). With the exception of the “epithelial-to-mesenchymal transition (EMT)-like cells” (cluster 12) that came from a single KPC tumor, all cell types were represented in all four KPC tumors (Supplementary Fig. S4G).

Analysis of Fibroblasts in KPC Tumors Reveals a Novel CAF Subtype with Antigen Presentation Features

To discern fibroblast heterogeneity, we next analyzed the fibroblast-enriched fraction isolated from each of the KPC tumors. We combined the sequencing data from the fibroblast-enriched populations isolated from the four KPC tumors into one data set consisting of 8,443 cells and analyzed them together. The fibroblast-enriched analysis resulted in 10 cell clusters, containing mostly EPCAM-negative ductal cells and fibroblasts (Fig. 4C; Supplementary Fig. S4H; Supplementary Table S19). Fibroblasts comprised half of

the cells detected, and segregated into two main clusters. An additional small cluster of fibroblasts was identified as lipofibroblasts, a lineage of lipid droplet-containing fibroblasts coexpressing lipid metabolism genes such as *Fabp4* and *Car3* (Fig. 4C, cluster 7; Supplementary Table S20; ref. 56). To further characterize the fibroblast populations, we separately analyzed the cells from the two main fibroblast clusters (clusters 5 and 6; Fig. 4C), and plotted these cells on a t-SNE plot (Fig. 4D). The 4,012 fibroblasts formed three subclusters, each with distinct gene signatures (Fig. 4D and E; Supplementary Fig. S4I; Supplementary Table S21). Subclusters 1 and 3 expressed marker genes that were very similar to the human iCAF and myCAF signatures, respectively (Fig. 4E; Supplementary Table S22). The iCAF subcluster (subcluster 1) was rich in the lectin *Clec3b*, as well as in chemokines and other inflammatory mediators such as *Il6*, *Cxcl1*, and *Ly6c1* (Fig. 4E and F; Supplementary Table S22). Like human iCAFs, mouse iCAFs expressed higher levels of the hyaluronan synthase *Has1* and specific collagens (e.g., *Col14a1*), suggesting that iCAFs have specific functions in ECM deposition (Fig. 4F). The myCAF subcluster (subcluster 3) showed high expression of the smooth muscle genes *Acta2* and *Tagln*, as well as *Igfbp3*, *Thy1*, *Col12a1*, and *Tbbs2* (Fig. 4E and F; Supplementary Table S22). A cross-species comparison between marker genes of the different subtypes demonstrated concordance between human iCAFs and mouse iCAFs, as well as between human myCAFs and mouse myCAFs (Supplementary Fig. S4J and S4K). Subcluster 2 was distinct from both iCAFs and myCAFs and expressed genes belonging to the MHC class II family, which are usually restricted to antigen-presenting cells (APC) of the immune system (Fig. 4E and G; Supplementary Table S22). Examples of these genes are *H2-Aa* and *H2-Ab1*, encoding the alpha and beta chains, respectively, of MHC class II in C57BL/6 mice, and *Cd74*, encoding the invariant chain. We therefore named these cells “antigen-presenting CAFs” (apCAF). In addition to MHC class II-related genes, apCAFs expressed other unique markers such as *Saa3*, which was implicated as a protumorigenic factor in pancreatic CAFs (57), and *Slpi*, which was previously identified as a proinflammatory gene in dysplastic skin fibroblasts (Fig. 4E and G; ref. 14). apCAFs also expressed pan-fibroblast markers such as *Col1a1*, *Col1a2*, *Dcn*, and *Pdpr* at comparable levels to iCAFs and myCAFs, confirming that they are genuine fibroblasts (Fig. 4G). GSEA comparing all three CAF subtypes demonstrated upregulation of inflammatory pathways in mouse iCAFs (e.g., JAK/STAT signaling, cytokine interactions with their receptors and coagulation; Supplementary Fig. S5A; Supplementary Table S23). The pathways specifically upregulated in mouse myCAFs were EMT, myogenesis, ECM receptor interaction, and focal adhesion (Supplementary Fig. S5B; Supplementary Table S23). The pathways upregulated in iCAFs and myCAFs were similar to those found upregulated in human iCAFs and myCAFs, respectively, by GSEA, and to what we have previously showed *in vitro* and *in vivo* (16, 49). Many pathways were uniquely upregulated in the newly defined apCAF subtype, including antigen presentation and processing, fatty-acid metabolism, MYC targets, and MTORC1 signaling (Supplementary Fig. S5C; Supplementary Table S23).



Figure 4. Single-cell analysis of KPC tumors recapitulates human PDAC and reveals a novel CAF subtype. **A**, Unsupervised clustering of all viable cells from four KPC mouse PDAC tumors, represented as a t-SNE plot. Different cell type clusters are color coded. **B**, Bubble plot showing selected cell type-specific markers across all clusters. Size of dots represents fraction of cells expressing a particular marker, and intensity of color indicates level of mean expression. Legends are shown below. **C**, Unsupervised clustering of the fibroblast-enriched fraction from PDAC tumors of four KPC mice, represented as a t-SNE plot. Different cell type clusters are color coded. **D**, Unsupervised reclustering of the fibroblasts (clusters 5 and 6 from **C**) in the four KPC tumors, represented as a t-SNE plot. Different fibroblast subclusters are color coded. **E**, Heat map showing scaled normalized expression of discriminative marker genes between the three fibroblast subclusters, with cells as columns and genes as rows. Color scheme represents Z-score distribution from -3 (blue) to 3 (dark orange). **F**, Violin plots of selected iCAF and myCAF markers, showing normalized expression in each of the subclusters. **G**, Violin plots of selected apCAF and pan-CAF markers showing normalized expression in each of the subclusters. **H**, Heat map showing the top differentially activated proteins (red) in each CAF subtype, as predicted by VIPER analysis. Color scheme represents Z-score distribution from -2 (blue) to 2 (red).

To detect master regulators that are active in these three murine CAF subpopulations, we performed protein-activity analysis using the ARACNe and VIPER algorithms. Included among the most highly activated proteins in apCAFs were the MHCII-related genes *H2-Ab1* and *Cd74* (Fig. 4H; Supplementary Table S24). In addition, other regulators of immune activity were found upregulated in apCAFs. For example, BCAM (CD239) and F11R (CD321), members of the immunoglobulin superfamily, and IRF5—an interferon-regulating protein—were all differentially active in apCAFs (Fig. 4H). Compared with iCAFs and myCAFs, apCAFs also showed higher activity for STAT1, which is known to mediate MHCII expression in response to IFN γ (Supplementary Table S24). This suggests that apCAFs are regulated by IFN γ signaling *in vivo*. In addition, NFE2L2 and most prominently NFE2L3 (encoded by *Nrf2* and *Nrf3*, respectively) are specifically activated in apCAFs, indicating an antioxidant response in apCAFs (Fig. 4H; Supplementary Table S24). Mouse iCAFs show activity of IL6 and Ly6C1, as expected, among other inflammatory proteins (Fig. 4H; Supplementary Table S24). Mouse myCAFs show high activity of HEYL, SMAD2, SNAI1, and TWIST2, as well as myCAF characteristic proteins such as PDGFR β and several myosins (Fig. 4H; Supplementary Table S24). We also identified CD34 and FAP as proteins that are differentially active in iCAFs and myCAFs, respectively (Fig. 4H; Supplementary Table S24).

MHCII Is Expressed in Mouse CAFs

Having identified the surface protein PDPN as a pan-CAF marker by single-cell RNA-seq, we used IHC to validate PDPN expression in all CAFs in autochthonous pancreatic intraepithelial neoplasia and PDAC lesions in KPC mice, and in PDAC tumors generated from orthotopically transplanted KPC-derived organoids (Supplementary Fig. S6A; ref. 58). To further validate the inclusivity and specificity of PDPN as a CAF marker, we used the PDPN antibody to isolate CAFs from single-cell suspensions of KPC tumors using FACS. Antibodies against CD45, CD31, EPCAM, and E-cadherin were used to eliminate other cell types, prior to sorting PDPN-positive cells (Supplementary Fig. S6B). RNA was isolated, and gene expression was measured by qPCR in PDPN-positive cells compared with unsorted tumor cells. Pan-CAF markers (*Col1a1* and *Col4a1*) as well as a subset of myCAF and iCAF markers were enriched in the PDPN-positive population (Supplementary Fig. S6C and S6D). MHCII genes (*H2-Ab1* and *Cd74*) were also detected in PDPN-positive cells, but these were expressed at substantially lower levels compared with the unsorted cells, which contained immune cells (Supplementary Fig. S6E). Other apCAF markers (e.g., *Slpi* and *Saa3*) were expressed at slightly higher levels in PDPN-positive cells (Supplementary Fig. S6E). Thus, the PDPN-positive population broadly represents CAFs in KPC tumors.

To validate the expression of MHCII genes in CAFs, we used RNA *in situ* hybridization (ISH) to simultaneously detect *H2-Ab1* and *Col1a1* transcripts in KPC tumor sections. In addition to many single positive cells, representing either APCs (*H2-Ab1*-positive) or other CAFs (*Col1a1*-positive), we also detected cells that expressed both transcripts, consistent with the presence of apCAFs in murine PDAC (Fig. 5A). Addi-

tionally, sequential IHC of CD74 and PDPN demonstrated a fraction of stromal cells expressing both markers, providing further confirmation for the presence of apCAFs in KPC tumors (Fig. 5B).

Isolation of Three CAF Subtypes by Flow Cytometry

To isolate and characterize apCAFs and other CAF subpopulations, we examined our single-cell data and identified surface proteins that were uniquely expressed in each CAF subpopulation. In addition to MHCII, which was unique to apCAFs, we identified Ly6C as an iCAF-specific surface marker (see Fig. 4E; Supplementary Table S22). Following the exclusion of immune and epithelial cells, we gated on PDPN-positive cells. Using anti-Ly6C and anti-MHCII antibodies, PDPN-positive cells segregated into three populations: (i) Ly6C-positive, (ii) MHCII-positive, and (iii) MHCII/Ly6C-double negative, presumably corresponding to iCAFs, apCAFs, and myCAFs, respectively (Fig. 5C). Flow cytometry analysis of 20 KPC tumors showed an average of 44.4% iCAFs, 45.3% myCAFs, and 10.3% apCAFs within the PDPN-positive population (Fig. 5D). To validate this strategy for CAF sorting, qPCR analysis was performed on RNA prepared from cells isolated accordingly by FACS. All three CAF subpopulations showed high expression of the pan-fibroblast markers *Col1a1*, *Col4a1*, *Dcn*, and *Pdpn*, compared with CD45-positive cells that were sorted concurrently (Supplementary Fig. S6F). MHCII-positive CAFs were unique in their high expression of *Cd74* and *H2-Ab1*, as well as the apCAF markers *Slpi* and *Saa3* (Fig. 5E). Ly6C-positive cells showed high relative expression of the iCAF markers *Il6*, *Cxcl12*, and *Pi16* (Fig. 5F). Finally, cells that were negative for both MHCII and Ly6C showed significantly higher relative expression of the myCAF markers *Acta2* and *Tgfb1*, suggesting an enrichment of myCAFs in this population (Fig. 5G).

Although apCAFs were identified as a subtype of fibroblasts in KPC tumors, they differed from myCAFs and iCAFs in expression of genes that are also found in the ductal cancer cell clusters, such as *Msln*, *Clu*, and *Krt19* (Fig. 4E; Supplementary Table S22), raising the possibility that apCAFs arise from cancer cells that have undergone EMT. To test this, we isolated the different CAF subtypes by FACS, prepared DNA from the cells and performed PCR genotyping. Although EPCAM-positive cancer cells sorted from the tumors harbored both the mutant and wild-type alleles of *Kras*^{G12D} and the mutant allele of *Trp53*^{R172H}, none of the CAF subpopulations harbored mutant *Kras* or *Trp53* alleles, confirming their mesenchymal origin (Supplementary Fig. S6G).

apCAFs Are Detectable in Human PDAC

Following the identification of apCAFs in mouse PDAC tumors, we looked for evidence of these cells in our human single-cell data. We detected subsets of human CAFs expressing modest levels of the human leukocyte antigen (HLA) genes that encode MHCII chains (*HLA-DRA*, *HLA-DPA1*, and *HLA-DQA1*; Fig. 6A). These subsets also expressed *CD74*, which encodes the invariant chain, and *SLPI*, which is one of the prominent apCAF markers in mouse PDAC tumors (Fig. 6A). We found that 20.9% of the human CAFs coexpressed

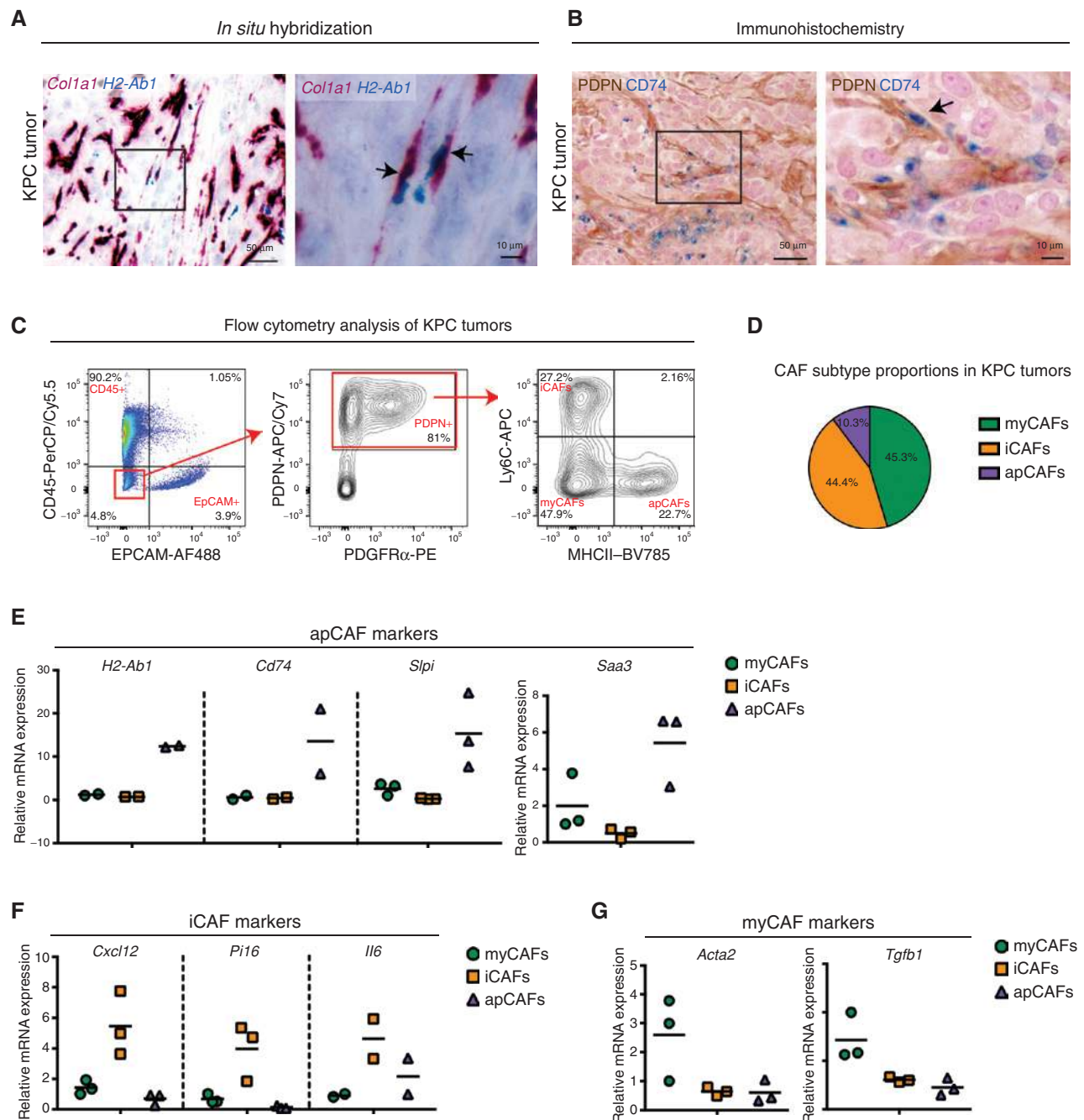


Figure 5. MHCII expression characterizes a third CAF subpopulation in KPC tumors. **A**, Duplex *in situ* hybridization of *Col1a1* and *H2-Ab1* in KPC tumor sections. The black square on the left is magnified in the right plot. Arrows indicate apCAFs. **B**, Sequential IHC of PDPN and CD74 in KPC tumor sections. The black square on the left is magnified in the right plot. Arrow indicates an apCAF. **C**, A representative flow cytometry analysis of cell suspension from a KPC tumor. Forward and side scatter were used to eliminate debris, and DAPI staining was used to eliminate dead cells. CD45 was used as an immune cell marker, EPCAM as an epithelial cell marker, and PDPN and PDGFR α as fibroblast markers. Cells that were negative for both CD45 and EPCAM (red square on the left), and positive for PDPN (red rectangle in the middle) were gated on for Ly6C and MHCII expression. The top left quarter shows iCAFs (Ly6C⁺, MHCII⁻), the bottom right quarter shows apCAFs (Ly6C⁻, MHCII⁺), and the bottom left quarter shows myCAFs (Ly6C⁻, MHCII⁻). **D**, Proportions of CAF subtypes from the PDPN-positive population in KPC tumors, as measured by flow cytometry analysis ($n = 20$, % \pm SEM: iCAFs 44.4 \pm 3.9, apCAFs 10.3 \pm 1.25, myCAFs 45.3 \pm 4.1). **E-G**, qPCR analysis of apCAF marker genes (**E**), iCAF marker genes (**F**), and myCAF marker genes (**G**) in the three CAF subtypes sorted from KPC tumors ($n \geq 2$ biological replicates). Black horizontal line represents mean value of data points. All transcripts were normalized to *Hprt*.

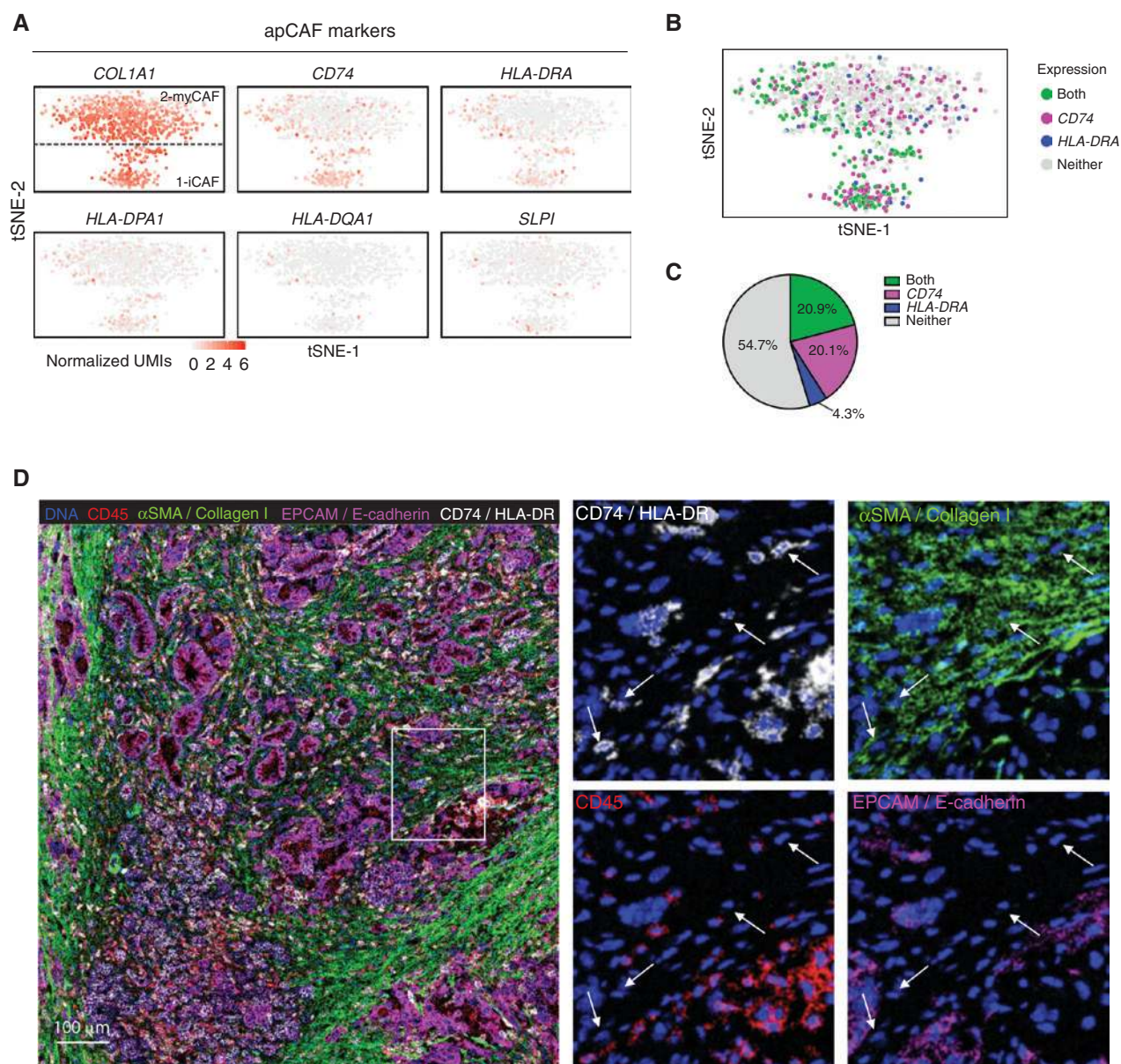


Figure 6. apCAFs are detectable in human PDAC. **A**, Expression levels of *COL1A1* and selected apCAF marker genes in the human CAF data set, represented as t-SNE plots. Legend shows a color gradient of normalized expression. Dotted line in the *COL1A1* t-SNE plot separates the iCAF and myCAF subclusters according to Fig. 3A. **B**, t-SNE plot showing binary expression scheme of *HLA-DRA* and *CD74* in human CAFs. Colors represent cells expressing *HLA-DRA* only (blue), *CD74* only (pink), both genes (green), or neither (gray). **C**, Quantification of the t-SNE plot shown in **B**. **D**, A representative image from an imaging mass cytometry staining of human PDAC sections, using metal-conjugated antibodies. Tumor sections from 4 different patients were stained. Left, a zoomed-out image. The small plots on the right show a magnification of the depicted area within the section (white rectangle), where each plot is stained for a specific marker(s), as indicated. Arrows are pointing to examples of apCAFs.

HLA-DRA and *CD74*, implying a capacity to generate a functional MHCII structure in some CAFs (Fig. 6B and C). These cells were predominantly admixed with the iCAF population (Fig. 6A and B), and did not form a separate cluster. Accordingly, the VIPER regulator analysis that we performed on human CAFs showed that master regulators belonging to the antigen presentation machinery such as *CD74* and *XBP1*—a transcription factor involved in the endoplasmic reticulum stress response that is known to regulate MHCII

genes (59, 60)—were differentially active in iCAFs (Fig. 3H and I), supporting the presence of apCAF traits in human PDAC. To confirm the existence of apCAFs in human PDAC, we costained human PDAC sections for the fibroblast marker *COL1A1* and the invariant chain *CD74* by RNA ISH, and identified cells that expressed both transcripts (Supplementary Fig. S7A). IHC staining of human PDAC sections for the fibroblast marker *PDGFRβ* and the MHCII molecules *HLA-DR/DP/DQ* further demonstrated the presence of apCAFs

in human PDAC (Supplementary Fig. S7B). Lastly, we performed imaging mass cytometry (IMC), combining multiple antibodies, and detected several examples of cells that coexpressed collagen I, CD74, and HLA-DR, but were devoid of CD45 or epithelial markers, corroborating their apCAF identity (Fig. 6D).

apCAFs Show Dynamic Features

We previously demonstrated that *in vitro*, myCAFs and iCAFs represent reversible cell states: iCAFs that are maintained in Matrigel with PDAC organoid-conditioned medium will convert to myfibroblasts if cultured in two-dimensional monolayer (2-D; ref. 16). We therefore sought to test whether apCAFs also have this inherent plasticity and can change into a different cell state given the appropriate culture conditions. To that end, we sorted apCAFs by FACS from KPC tumors and cultured them in 2-D. We compared gene expression between profiles of isolated apCAFs and 2-D-cultured apCAFs, and whereas CAFs in both conditions expressed comparable levels of the pan-CAF marker *Pdpm* (Supplementary Fig. S8A), tumor-derived apCAFs lost their MHCII expression, along with other apCAF markers, following 2-D culture (Fig. 7A; Supplementary Fig. S8B). Rather, sorted apCAFs cultured in 2-D upregulated myCAF markers, similar to myCAFs isolated from KPC tumors and cultured in 2-D (Fig. 7A; Supplementary Fig. S8B). Our results suggest that apCAFs are a dynamic fibroblast population and that they may require environmental cues to be maintained as a subpopulation.

apCAFs Can Present Antigens to T Cells

The presence of MHCII molecules on apCAFs suggests that this CAF subtype interacts with CD4⁺ T cells. To test this, we orthotopically transplanted KPC tumor organoids into the pancreata of MHCII-EGFP knock-in mice (Fig. 7B; ref. 61), and allowed PDAC tumors to form. We confirmed that pancreatic tumors that develop in the orthotopic model contain the three CAF subtypes, similar to the KPC model (Supplementary Fig. S8C). Next, we sorted by FACS the MHCII-expressing, GFP-positive CAFs as well as GFP-positive professional APCs from the transplanted tumors (Supplementary Fig. S8D). The presence of the GFP reporter allowed us to isolate MHCII-expressing cells without using an MHCII antibody, thus ensuring that the MHCII molecules remained intact. To test whether our sorted CAFs were capable of antigen presentation, we used the ovalbumin-specific TCR transgenic OTII mouse model (62), in which T cells are activated when presented with an OTII-specific ovalbumin peptide (OVA 323-339) by an APC. We incubated the sorted CAFs and professional APCs with the OVA peptide, and the OVA-loaded APCs and CAFs were cocultured with OTII-derived CD4⁺ T cells for 17 hours (Fig. 7B). Professional APCs from the MHCII-EGFP orthotopic model induced early activation markers of TCR ligation (CD25 and CD69) in cocultured T cells, in an OVA-specific manner (Fig. 7C and D). Whereas myCAFs and iCAFs did not induce a measurable T-cell activation when loaded with OVA, apCAFs isolated from the same orthotopic tumors demonstrated the capacity to induce CD25 and CD69 in cocultured T cells in an OVA-specific manner (Fig. 7C and D).

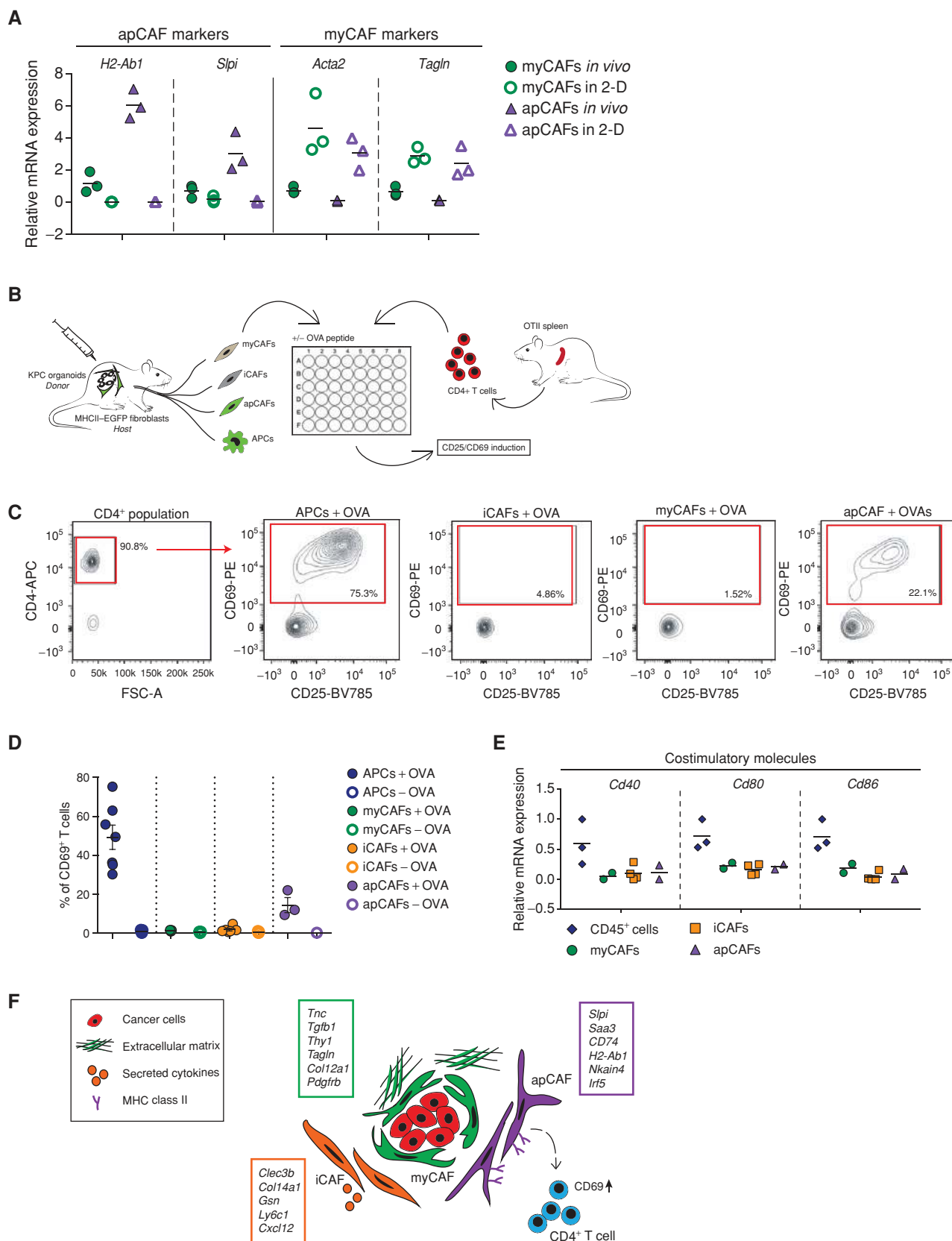
Professional APCs express costimulatory molecules on their cell surface, which provide the second signal necessary to induce CD4⁺ T-cell clonal proliferation following TCR ligation (63). Therefore, we examined whether, in addition to MHCII molecules, apCAFs also expressed genes encoding the costimulatory molecules CD80, CD86, and CD40. However, all CAF subtypes expressed low levels of the costimulatory genes compared with CD45-positive cells, with no differential expression for apCAFs over the other CAF subtypes (Fig. 7E). This suggests that apCAFs in PDAC play a different role compared with professional APCs *in vivo*.

DISCUSSION

In this study, we have used a droplet-based single-cell transcriptomics strategy to profile pancreatic tumors from human patients and KPC mice. We also used a negative depletion strategy upstream of transcriptome profiling to enrich for fibroblasts, enabling a more comprehensive analysis of heterogeneity within this population. Consistent with previous publications (64, 65), we identified numerous similarities between human PDAC and the tumors derived from the KPC mouse model, such as the predominance of macrophages over dendritic cells. Yet this cross-species comparison also identified differences between human PDAC and the mouse model that should be considered, such as differences in lymphocyte infiltration.

Previous studies have used single-cell transcriptomics to detail the composition of the normal human pancreas, focusing mostly on the endocrine lineages within the pancreatic islets, and the changes that occur during inflammation and aging (66–72). One of these studies focused on stellate cells, the resident fibroblasts of the pancreas, and identified two types of stellate cell activation in the normal pancreas, a standard activation and an immune activation, resembling the myCAF and iCAF classification (67). This suggests that physiologic conditions other than cancer may contribute to a heterogeneous fibroblast activation in the pancreas. By detailing the subpopulations of cells present in adjacent-normal and PDAC tissues, our work complements these studies and provides new information about the cell types associated with pancreatic malignancy.

A recent study performed single-cell RNA-seq analysis of four human intraductal papillary mucinous neoplasms of different grades and of two human PDAC samples, describing epithelial and stromal cell changes associated with carcinogenesis of the pancreas (73). Although this study provides a detailed description of the epithelial cells in preneoplastic and neoplastic conditions, the small number of stromal cells that was analyzed did not allow for a comprehensive delineation of the immune and fibroblast populations. Notably, the authors describe an abundance of myeloid cells with an immune-suppressive nature present in PDAC. Our study furthers this observation by highlighting several subpopulations of immune cells that were not detected in the previous study, such as NK cells, NKT cells, Tregs, and alternatively activated macrophages. Supporting our observation of iCAF and myCAF subpopulations, the authors of the previous study were able to identify these subpopulations in the two tested PDAC samples, albeit in different proportions than



we detected. This discrepancy could be attributed to lower number of cells analyzed, to differences in digestion methods, or to heterogeneity between the human tumors analyzed. Another recent preprint reported CAF subtypes in a different mouse model of PDAC and showed similar populations of iCAFs and myCAFs (74). This study also detected expression of MHCII-related genes; however, these were detected within the myCAF population, likely reflecting limited cell numbers in this study. Our work expands upon this study to show that the MHCII-expressing CAFs are a transcriptionally and functionally distinct subtype, which can be found in both mouse and human PDAC.

CAF heterogeneity has been reported in other tumor types as well. Two transcriptionally distinct CAF subtypes with differing α SMA expression were reported in patients with colorectal cancer, supporting our findings in PDAC (44). A distinct CAF subtype was shown to maintain the cancer stem cell niche and was correlated with chemoresistance and poor prognosis in patients with breast and lung cancers (75). Another subtype of breast cancer CAFs was shown to attract and induce Tregs (76). Moreover, a comparison between the fibroblasts of nonmalignant lung tissue and lung tumor tissue showed variability in the expression of collagens and transcription factors between fibroblast subtypes (77), similar to our observation. These examples demonstrate that functional heterogeneity among CAFs is a general feature of cancer, rather than a phenomenon specific to PDAC.

Our fibroblast analysis comprehensively evaluated the transcriptomes of the iCAF and myCAF subpopulations, which we had previously characterized (16), and provided novel marker genes for these cells (Fig. 7F). The VIPER master regulator analysis further implies that iCAFs and myCAFs take on diverse functions *in vivo*. Our study identifies AGTR1 as a marker for the iCAF population. This receptor is a leading target in active clinical investigations for patients with PDAC (NCT01821729 and NCT03563248). An inhibitor of this receptor, Losartan, was shown to reduce intratumoral solid stress, leading to increased vascular perfusion and improved drug delivery (48, 78). A major source of solid stress in PDAC tumors is hyaluronan (7), and the enzymes responsible for hyaluronan production are uniquely and specifically expressed in iCAFs (*HAS1* and *HAS2* in the human data; *Has1* and *Has2* in the mouse data). Our data suggest that the iCAF

population, which is predicted to mediate solid stress in the tumor, would be targeted by Losartan. Therefore, in addition to the inflammatory signals we previously characterized as potential mediators of immune suppression, iCAF targeting may also be responsible for the efficacy of Losartan in treating PDAC.

Our work also uncovered a novel CAF subpopulation, apCAFs, which expresses MHCII molecules and has the capacity to present a model antigen to CD4⁺ T cells *ex vivo* (Fig. 7F). However, apCAFs lack the costimulatory molecules needed to induce T-cell proliferation. Therefore, we hypothesize that the MHCII expressed by apCAFs acts as a decoy receptor to deactivate CD4⁺ T cells by inducing either anergy or differentiation into Tregs. In this case, apCAFs are expected to decrease the CD8⁺ to Treg ratio and curtail antitumor immunity. apCAFs thus might contribute to immune suppression in the PDAC microenvironment. Stromal cells of the lymph node have been shown to induce apoptosis of CD4⁺ T cells and reduce their efficiency to restimulate, in a mechanism involving peptide-MHCII complexes acquired from DCs (79). In another report, lymph node stromal cells induced CD4⁺ T-cell population contraction in an H2-Ab1-dependent manner (80). These examples support the premise that stromal cells have the capacity to act as nonprofessional APCs, in a manner that inhibits optimal T-cell response.

We have previously reported on the ability of the iCAF and myCAF populations to interconvert (16). Similarly, apCAFs can differentiate into myCAFs upon culture, demonstrating that apCAFs are also a dynamic cell state. CAF plasticity can potentially be exploited to therapeutically promote the conversion of protumorigenic CAFs into antitumorigenic ones, and to modulate CAF activity in the tumor (49). Further investigation is required in order to determine the intratumoral signals that induce apCAF formation and activation, and to define the role(s) that each CAF subtype plays in the PDAC microenvironment and tumor immunity.

METHODS

Human Samples and Mouse Models

Human PDAC resection specimens were obtained from the Sidney Kimmel Comprehensive Cancer Center at Johns Hopkins University

Figure 7. apCAFs can present antigens to T cells. **A**, qPCR analysis of apCAF and myCAF marker genes in apCAFs sorted from KPC tumors (apCAFs *in vivo*) compared with the same population following culture in two-dimensional monolayer (apCAFs in 2-D). myCAFs sorted from the same KPC tumors (myCAFs *in vivo*) and myCAFs grown in 2-D (myCAFs in 2-D) were used as positive controls for myCAF genes ($n = 3$ biological replicates). Black horizontal line represents mean value of data points. All transcripts were normalized to *Hprt*. **B**, An illustration of the T-cell activation assay: the three CAF subtypes and professional APCs were isolated from orthotopic tumors that were transplanted in MHCII-EGFP host mice (left). Sorted cells were incubated with or without OVA peptide, and then cocultured with CD4⁺ T cells that were isolated from OVA-specific OTII mice (right). After 17 hours of coculture, T cells were analyzed by flow cytometry for early activation markers. **C**, An example of T-cell early activation assay. CD4⁺ T cells that were cocultured with OVA-loaded APCs or different CAF subtypes for 17 hours were washed and stained for T-cell markers, and read on a flow cytometer. Debris and dead cells were excluded by forward and side scatter and by DAPI staining (not shown). Viable cells were stained for CD4, CD25, and CD69. A representative example of CD4 gating is shown on the leftmost plot. Each of the other plots shows the CD69⁺ population upon coculture of T cells with different cell types, following an incubation with OVA. **D**, Quantification of three independent experiments of T-cell early activation. Values \pm SEM are shown ($n = 7$ for APCs and myCAFs; $n = 6$ for iCAFs; $n = 3$ for apCAFs). **E**, qPCR analysis of costimulatory molecules in the three CAF subtypes sorted from KPC tumors, compared with CD45⁺ cells sorted from the same tumors ($n \geq 2$ biological replicates). Black horizontal line represents mean value of data points. All transcripts were normalized to *Hprt*. **F**, Illustrated summary of CAF subpopulations and their functions in PDAC. Subpopulations and their unique features are highlighted by different colors: myCAFs in green, iCAFs in orange, and apCAFs in purple. Selected markers of each subpopulation are listed in the corresponding boxes.

and from the Memorial Sloan Kettering Cancer Center. All tissue donations and experiments were reviewed and approved by the Institutional Review Board of Cold Spring Harbor Laboratory and the clinical institutions involved. Written informed consent was obtained prior to acquisition of tissue from all patients. The studies were conducted in accordance with ethical guidelines (Declaration of Helsinki). Samples were confirmed to be tumor or adjacent-normal based on pathologist assessment. KPC (*Kras*^{G12D}/LSL-G12D; *Trp53*^{R172H}/LSL-R172H; *Pdx1-Cre*) mice were previously described (54). MHCII-EGFP mice (MGI ID: 2387946, Symbol: H2-Ab1^{tm1Hpl}; ref. 61) were obtained from the lab of Hidde Ploegh at Boston Children's Hospital. Orthotopic transplantation of KPC-derived organoids into MHCII-EGFP mice was performed as previously described (58). B6.Cg-Tg(TcrαTcrβ)425Cbn/J (OTII) mice were purchased from The Jackson Laboratory (stock # 004194; ref. 62). All animal procedures and studies were conducted in accordance with the Institutional Animal Care and Use Committee at Cold Spring Harbor Laboratory.

Sample Preparation, Staining, and Sorting for Single-Cell RNA-seq

Tumor specimens from human patients and from KPC mice were minced and enzymatically digested in 10% FBS/DMEM supplemented with Collagenase D (Sigma #11088882001, 2.5 mg/mL), Liberase DL (Sigma #5466202001, 0.5 mg/mL), and DNase I (Sigma, D5025, 0.2 mg/mL) for 45 minutes at 37°C with agitation. Adjacent-normal specimens from human patients were minced and digested in Human Normal Organoid media (58) supplemented with Collagenase XI (Sigma C7657, 5 mg/mL), Y-27632 (STEMCELL Technologies, 10.5 μmol/L), and DNase I (Sigma #D5025, 10 μg/mL) for 3 cycles of 8 minutes at 37°C with agitation. After each cycle, tissue pieces were let to settle down by gravity, and supernatant was collected and quenched by excess advanced DMEM/F12 (#12634-010) supplemented with 1× GlutaMAX (Gibco #35050-061), 10 mmol/L HEPES (Gibco #15630-080), and 1% of penicillin/streptomycin. Fresh digestion media were applied to the remaining tissue for the next digestion cycle, and cells collected from each cycle were merged into one sample. Cell digestion of both tumor and adjacent-normal samples was strained through a 100-μm cell strainer and quenched with 2% FBS/PBS. The solution was spun down, and cells were resuspended in ACK lysis buffer to eliminate red blood cells. After a 3-minute incubation on ice, the ACK was quenched with 2% FBS/PBS. Cells were spun down, resuspended in PBS supplemented with 0.5% BSA and 2 mmol/L EDTA, and blocked with human FcR binding inhibitor (for human tissue, eBioscience #14-9161-73, 1:5) or with anti-mouse CD16/CD32 Fc Block (for mouse tissue, BioLegend, clone 2.4G2, 1:50) for 15 minutes at 4°C. Staining of human tissue was performed with the following antibodies: CD45-AF647 (BioLegend, clone H130, 1:20), CD31-AF647 (BioLegend, clone WM59, 1:20), and EPCAM-AF647 (BioLegend, clone 9C4, 1:20) for 30 minutes at 4°C. Staining of mouse tissue was performed with the following antibodies: CD45-AF647 (BioLegend, clone 30-F11, 1:20), CD31-AF647 (BioLegend, clone 390, 1:20), and EPCAM-AF647 (BioLegend, clone G8.8, 1:20) for 30 minutes at 4°C. Prior to sorting, DAPI was added to cell suspension (Sigma #D8417, 1 μg/mL). Cells were sorted using BD FACSAria Fusion instrument and collected in 20% FBS/PBS. Following exclusion of debris, 50,000 to 100,000 DAPI-negative cells were collected from each sample (for “viable cell” fraction). When enough cells were available, sorting for DAPI-, CD45-, CD31-, and EPCAM-negative cells was performed (for “fibroblast-enriched” fraction).

Single-Cell Capture, Library Preparation, and RNA-seq

Sorted cells were washed and resuspended in PBS containing 0.04% BSA. Cells were counted on Countess II automated cell counter (Thermo Fisher), and up to 12,000 cells were loaded per lane on

10X Chromium microfluidic chips. Single-cell capture, barcoding, and library preparation were performed using the 10X Chromium version 2 chemistry, and according to the manufacturer's protocol (#CG00052). cDNA and libraries were checked for quality on Agilent 4200 TapeStation and quantified by KAPA qPCR before sequencing on a single lane of a HiSeq4000 (Illumina) to an average depth of 50,000 reads per cell.

Single-Cell Data Processing, Quality Control, and Analysis

The Cell Ranger pipeline (v1.3, 10X Genomics) was used to convert Illumina base call files to FASTQ files, align FASTQs to the hg19 reference (v1.2.0, 10X Genomics) for human samples and mm10 reference (v1.2.0, 10X Genomics) for mouse samples, and produce a digital gene-cell counts matrix. Samples were combined using the Cell Ranger aggregate function, which subsamples digital counts matrices such that the number of confidently mapped transcriptomic reads is equal among all samples and creates a unified digital counts matrix. Gene-cell matrices were filtered to remove cells with fewer than 500 transcripts and genes with fewer than two counts in two cells. The gene-cell matrices were then normalized such that the number of unique molecular identifiers (UMI) in each cell is equal to the median UMI count across the data set and log transformed. Expression at 1,000 highly variable genes in each data set, selected as the genes with the highest dispersion, was used to reduce the dimensionality of the data sets to three dimensions using Barnes Hut approximate t-SNE (BH t-SNE; ref. 81) and cells were clustered using density-based spatial clustering of applications with noise (DBSCAN; ref. 82) in t-SNE space (25). Cells that were not assigned cluster labels by DBSCAN were discarded from further analysis. Cluster marker genes were identified using one-vs-rest binary classification metrics. Briefly, for a given cluster, log mean expression of each gene was computed and compared with the log mean expression of that gene in cells outside the cluster. Genes with a log-fold difference in mean expression greater than 2 were used to construct receiver operator characteristic curves (ROC) and the area under the ROC was used to rank putative marker genes. These marker genes were used to assign cellular identities to clusters. Certain cell populations were subclustered by repeating the procedure described above. Interactive analysis was done using the CellView RShiny web application (83). The mouse RNA-seq data are available at the Gene Expression Omnibus under the accession number GSE129455. The human RNA-seq data are available at NCBI dbGaP under the accession number phs001840.v1.p1.

Key Resources for Single-Cell Analysis

Key resources for single-cell analysis include: (i) 10X Cell Ranger software: version 1.3.0, md5sum: f399da7266d8d61036bd29851dcf8244 (<https://support.10xgenomics.com/single-cell-gene-expression/software/downloads/1.3/>); (ii) 10X hg19 reference genome: version 1.2.0, md5sum: 74608d0a6fdd8c10e2918339a30c3c49 (<https://support.10xgenomics.com/single-cell-gene-expression/software/downloads/1.3/>); and (iii) 10X mm10 reference genome: version 1.2.0, md5sum: 6c8701a83c7b66ca123a6b4f149bec26 (<https://support.10xgenomics.com/single-cell-gene-expression/software/downloads/1.3/>).

Context-Specific Regulatory Model and Master Regulator Analysis of Human and Mouse CAFs

Human and mouse context-specific regulatory networks were reverse engineered by ARACNe (84) from human and mouse single-cell gene-expression profiles, respectively. ARACNe was run with 200 bootstrap iterations using 1,824 transcription factors (genes annotated in the gene ontology molecular function database as GO:0003700, “transcription factor activity,” or as GO:0003677, “DNA binding,” and GO:0030528, “transcription regulator activity,” or as GO:00034677 and GO:0045449, “regulation of transcription”) and 3,477 signaling

pathway-related genes (annotated in the GO biological process database as GO:0007165 “signal transduction” and in the GO cellular component database as GO:0005622, “intracellular,” or GO:0005886, “plasma membrane”). The human CAF network has been generated from iCAF and myCAF cells previously identified based on gene-expression markers (iCAF signature genes: *IL6*, *PDGFRA*, *CFD*, *PLA2G2A*, *HAS1*, *CXCL2*, *CCL2*, *CLU*, *EMP1*, *LMNA*; myCAF signature genes: *TAGLN*, *ACTA2*, *MMP11*, *PDGFRB*, *HOPX*, and *POSTN*). The mouse CAF network has been generated from iCAFs, myCAFs, and apCAFs previously identified based on gene-expression markers (Supplementary Table S22). The regulatory models for human and mouse CAFs were generated from the ARACNe networks using the VIPER package (50). The most representative cells of each CAF subtype were identified in each cluster using the silhouette analysis (silhouette widths > 0.36 for human and silhouette widths > 0.3 for mouse), and used for the master regulator analysis. The master regulator analysis was performed by comparing each CAF subtype against the others using the msviper algorithm of the VIPER package.

In Situ Hybridization and IHC

Tissues were fixed in 10% normal buffered formalin for 16 to 24 hours. Tissues were embedded in paraffin, and 5- μ m sections were cut and mounted on slides. Slides were rehydrated through histoclear and ethanol series, and antigen retrieval was performed in 10 mmol/L citrate buffer, in a pressure cooker for 6 minutes. Tissues were blocked in 2.5% Normal Horse Serum blocking solution (Vector Laboratories #S-2012) and subjected to staining with the following antibodies: Podoplanin-biotin (BioLegend, clone 8.1.1, 1:200) and CD74 (BioLegend, clone In1/CD74 1:200) for mouse sections, and HLA-DR, DP, DQ (Thermo Fisher Scientific, clone CR3/43, 1:50), and PDGFR β (Abcam #ab32570 1:400) for human sections. Horseradish peroxidase (HRP)-streptavidin (Vector Laboratories #SA-5704), ImmPRESS alkaline phosphatase anti-Rat IgG polymer (Vector Laboratories #MP-5444), ImmPRESS alkaline phosphatase anti-mouse IgG polymer (Vector Laboratories #MP-5402), and ImmPRESS HRP anti-Rabbit IgG polymer (Vector Laboratories #MP-7401) were used as secondary antibodies. ImmPACT DAB peroxidase substrate (Vector Laboratories #SK-4105) and Vector Blue Alkaline Phosphatase substrate (Vector Laboratories #SK-5300) were used as substrates. Hematoxylin (Vector Laboratories #H-3404) and Nuclear Fast Red (Vector Laboratories #H-3403) were used as counterstains. ISH was performed using the RNAscope 2.5 HD duplex assay (ACD) according to the manufacturer's instructions. RNAscope probes used were Mm-H2-Ab1 (#414731) and Mm-Col1a1-C2 (#319371-C2) for mouse sections, and Hs-CD74 (#477521) and Hs-COL1A1-C2 (#401891-C2) for human sections.

Multiplexed Imaging by IMC

Formalin-fixed paraffin-embedded human PDAC tissues were cut into 5- μ m sections and mounted on slides. Slides were incubated for 15 minutes at 55°C in a dry oven, deparaffinized in fresh histoclear, and rehydrated through a series of graded alcohols. Antigen retrieval was performed in a decloaking chamber (BioSB TintoRetriever) for 15 minutes at 95°C in Tris-EDTA, pH 9.2. After blocking in buffer containing 3% BSA, slides were incubated overnight at 4°C with a cocktail of metal-conjugated IMC-validated primary antibodies: CD45-89Y (clone HI30), α SMA-141Pr (clone 1A4), CD74-155Gd (clone LN2), HLA-DR-159Tb (clone LN3), EPCAM-158Gd (clone 9C4), E-cadherin-158Gd (clone 4A2), and collagen I-169Tm (polyclonal). The following day, slides were washed twice in Dulbecco's Phosphate-Buffered Saline and counterstained with iridium intercalator (0.25 μ mol/L) for 5 minutes at room temperature, to visualize the DNA. After a final wash in ddH₂O, the slides were air-dried for 20 minutes. The slides were then loaded on the Fluidigm Hyperion imaging mass cytometer. Regions of interest were selected using the acquisition software and ablated by

the Hyperion. The resulting images were exported as 16-bit .tiff files using the Fluidigm MCDViewer software and analyzed using the open source Histocat++ toolbox (85).

Flow Cytometry and Sorting of KPC CAFs

KPC mouse tumors were digested and single-cell suspensions were prepared as described above for human tumors. Cells were resuspended in 2% FBS/PBS and blocked with anti-mouse CD16/CD32 Fc block for 15 minutes at 4°C (BioLegend, clone 2.4G2, 1:50). The following antibodies were used in the different flow experiments (all from BioLegend at 1:200): CD45 (clone 30-F11), CD31 (clone 390), EPCAM (clone G8.8), E-cadherin (clone DECMA-1), podoplanin (clone 8.1.1), CD140a (PDGFR α ; clone APA5), Ly6C (clone HK1.4), and I-A/I-E (MHCII; clone M5/114.15.2). Staining with antibodies was performed for 30 minutes at 4°C. Prior to flow cytometry, DAPI was added to cell suspension (Sigma #D8417, 1 μ g/mL). From each sample, 250,000 events were acquired on the BD LSRFortessa. Cell sorting was done on the FACSARIA II (CSHL), using the same antibodies as indicated for flow. Sorted cells were collected into 10% FBS/DMEM at 4°C.

RNA Preparation and qPCR

Sorted cells were spun down and pellets were resuspended in TRIzol. RNA was prepared by combining the standard TRIzol/chloroform extraction method with the PureLink RNA mini kit (Thermo Fisher Scientific #12183018A). cDNA was prepared using the TaqMan reverse transcription reagents (Thermo Fisher Scientific #N8080234), and qPCR was performed with TaqMan Universal Master Mix II without UNG (Thermo Fisher Scientific #4440047) on a QuantStudio 6 Flex Real-Time PCR system (Thermo Fisher Scientific). TaqMan probes that were used for qPCR: Cd74 (Mm00658576_m1), H2-Ab1 (Mm00439216_m1), Slpi (Mm00441530_g1), Saa3 (Mm00441203_m1), Il6 (Mm00446190_m1), Cxcl12 (Mm00445553_m1), Pi16 (Mm00470084_m1), Acta2 (Mm01546133_m1), Tgfb1 (Mm01178820_m1), Cd40 (Mm00441891_m1), Cd80 (Mm00711660_m1), Cd86 (Mm00444540_m1), Pdpn (Mm01348912_g1), Tagln (Mm00441661_g1), Myl9 (Mm01251442_m1), Col1a1 (Mm00801666_g1), Col4a1 (Mm01210125_m1), Dcn (Mm00514535_m1).

GSEA

GSEA (86) was performed between subclusters of human and mouse fibroblasts. The rank is based on differentially expressed genes between the subclusters, as computed with edgeR (87) for mouse samples and monocle (88) for human samples. The database used by GSEA is Molecular Signatures Database v6.1. Genes that were expressed in less than 10% of the cells in a given mouse subcluster or in less than 25% in a given human subcluster were filtered out of the analysis.

Genotyping of Sorted CAFs

DNA from sorted cells was prepared using the QIAamp DNA micro kit (Qiagen #56304). PCR was performed using standard protocols with the following primers for KRAS locus: forward primer: 5'-GGGTAGGTGTTGGGATAGCTG-3', reverse primer: 5'-TCCGAATTTCAGTGACTACAGATGTACAGAG-3'; and the following primers for p53 locus: forward primer: 5'-AGCCTGCCTAGCTTCCTCAGG-3', reverse primer: 5'-CTTGGAGACATAGCCACACTG-3'. PCR products were evaluated on ethidium bromide gel.

OTII CD4⁺ T-cell Enrichment and Early Activation Assay

Different CAF subtypes and CD45-positive APCs were isolated by FACS from tumors transplanted in MHCII-EGFP host mice. apCAFs and APCs were sorted by their GFP fluorescence. Between

13,000 and 25,000 sorted cells were incubated with 25 $\mu\text{g/mL}$ OVA peptide 323–339 or without a peptide, in 10% FBS/DMEM for 3 hours in U-bottom 96-well plates, in a standard 37°C 5% CO_2 humid incubator. Lymphocytes were isolated from the spleen of OTII mice and were enriched for CD4^+ T cells by negative selection using the MojoSort mouse CD4^+ T-cell isolation kit (BioLegend #480006). APC/CAF plates were washed twice, 50,000 CD4^+ T cells were coplated in 10% FBS/DMEM in each well, and plates were placed back in the incubator for 17 hours. Cells were then washed in 2% FBS/PBS, blocked in CD16/CD32 Fc Block (BioLegend, clone 2.4G2, 1:50), and stained with the following antibodies (all from BioLegend at 1:200): CD4 (clone RM4-5), CD25 (clone PC61), and CD69 (clone H1.2F3) for 30 minutes at 4°C. DAPI (Sigma #D8417, 1 $\mu\text{g/mL}$) was added to cell suspension prior to reading on the cytometer.

Disclosure of Potential Conflicts of Interest

K.H. Yu reports receiving commercial research support from Halozyme and BMS, is a consultant/advisory board member for Ipsen and Halozyme, and has received other remuneration from West-Ward Pharmaceuticals. E.M. Jaffee is Chief Medical Advisor at Lustgarten Foundation, reports receiving commercial research grants from Amgen, AduroBiotech, Bristol-Myers Squibb, and Hertz, has ownership interest (including stock, patents, etc.) in AduroBiotech, and is a consultant/advisory board member for CStone, DragonFly, and Genocoe. A. Califano has ownership interest (including stock, patents, etc.) in DarwinHealth and is a consultant/advisory board member for the same. D.A. Tuveson reports receiving commercial research grants from Fibrogen and ONO, has ownership interest (including stock, patents, etc.) in Leap Therapeutics and Surface Oncology, and is a consultant/advisory board member for Leap Oncology, Surface Oncology, ONO Therapeutics, Eli Lilly, and Bethyl Antibodies. No potential conflicts of interest were disclosed by the other authors.

Authors' Contributions

Conception and design: E. Elyada, R.A. Burkhardt, T.D. Armstrong, E.M. Jaffee, A. Califano, P. Robson, D.A. Tuveson

Development of methodology: E. Elyada, M. Bolisetty, S. Sivajothi, T.D. Armstrong, E.M. Jaffee

Acquisition of data (provided animals, acquired and managed patients, provided facilities, etc.): E. Elyada, M. Bolisetty, E.T. Courtois, R.A. Burkhardt, J.A. Teinor, S. Sivajothi, D.D. Engle, K.H. Yu, P. Robson

Analysis and interpretation of data (e.g., statistical analysis, biostatistics, computational analysis): E. Elyada, M. Bolisetty, P. Laise, W.F. Flynn, E.T. Courtois, R.A. Burkhardt, P. Belleau, G. Biffi, M.S. Lucito, S. Sivajothi, D.D. Engle, Y. Hao, C.L. Wolfgang, J. Preall, E.M. Jaffee, A. Califano, P. Robson, D.A. Tuveson

Writing, review, and/or revision of the manuscript: E. Elyada, W.F. Flynn, E.T. Courtois, G. Biffi, D.D. Engle, K.H. Yu, C.L. Wolfgang, Y. Park, E.M. Jaffee, P. Robson, D.A. Tuveson

Administrative, technical, or material support (i.e., reporting or organizing data, constructing databases): E. Elyada, C.L. Wolfgang, Y. Park, P. Robson

Study supervision: A. Califano, P. Robson, D.A. Tuveson

Acknowledgments

We would like to thank Hidde Ploegh for the MHCII-EGFP mice, Douglas Fearon and Ronald Evans for helpful insights and discussion, Arnaud Pommier, Naishitha Anaparthi, Morgan Truitt, Semir Beyaz, Michael Pickup, and Min Yao for their experiment suggestions and discussion, Richard Moffitt for his help with data analysis, Astrid

Deschenes and Anthony Carcio for technical help, and Lindsey Baker and Tobiloba Oni for critical reading of the manuscript. This work was supported by the Lustgarten Foundation, where D.A. Tuveson is a distinguished scholar and Director of the Lustgarten Foundation Dedicated Laboratory of Pancreatic Cancer Research. D.A. Tuveson is also supported by the Cold Spring Harbor Laboratory Association, the David Rubinstein Center for Pancreatic Cancer Research at MSKCC, the V Foundation, the Thompson Foundation, and the Simons Foundation (552716). In addition, this work was supported by the National Institutes of Health, NIH P30CA045508, P50CA101955, P20CA192996, U10CA180944, U01CA168409, U01CA210240, R33CA206949, R01CA188134, and R01CA190092 to D.A. Tuveson and U01CA224013 to P. Robson and D.A. Tuveson. P. Robson is also supported by JAX laboratory startup funds and the JAX Cancer Center Support Grant (CCSG) P30CA034196-30. A. Califano is supported by the NCI Outstanding Investigator Award (R35 CA197745), the NCI Cancer Systems Biology Consortium (U54 CA209997), and two NIH Shared Instrumentation Grants (S10 OD012351, S10 OD0217640). A. Califano is also supported in part through the NCI Cancer Center Support Grant (P30 CA013696). E.M. Jaffee is supported by the James W. and Frances Gibson McGlothlin Foundation, the Skip Viragh Center for Pancreatic Cancer at Johns Hopkins, the Bloomberg-Kimmel Institute for Cancer Immunotherapy at Johns Hopkins, the National Cancer Institute (R01 CA18492-04 and R01 CA19729603), and by a Stand Up To Cancer–Lustgarten Foundation Pancreatic Cancer Convergence Translational Research Grant (SU2C-AACR-DT14-14). C.L. Wolfgang is supported by the NIH (R01CA182076). R.A. Burkhardt is supported by a Stand Up To Cancer–Lustgarten Foundation Pancreatic Cancer Interception Translational Cancer Research Grant (grant number SU2C-AACR-DT26-17). Stand Up To Cancer (SU2C) is a division of the Entertainment Industry Foundation administered by the American Association for Cancer Research, the Scientific Partner of SU2C. We also thank the Cold Spring Harbor Laboratory shared resources: P. Moody and C. Kanzler at the flow cytometry facility, C. Regan at the single-cell core, the animal facility, the histology core, the bioinformatics core, and the microscopy core. These shared resources are funded by the NIH Cancer Center Support Grant P30CA045508. In addition, we are grateful for support from the following: The Cold Spring Harbor Laboratory and Northwell Health Affiliation (for J. Preall and D.A. Tuveson), the Human Frontiers Science Program (LT000403/2014-L for E. Elyada and LT000195/2015-L for G. Biffi), EMBO (ALTF 1203-2014 for G. Biffi), NCI (R01 CA202762 for K.H. Yu, 5T32CA148056 and 5K99CA204725 for D.D. Engle), and the NIH (R50 CA211506-02 for Y. Park).

Received January 22, 2019; revised April 18, 2019; accepted May 30, 2019; published first June 13, 2019.

REFERENCES

1. Siegel RL, Miller KD, Jemal A. Cancer statistics, 2018. *CA Cancer J Clin* 2018;68:7–30.
2. Waghray M, Yalamanchili M, di Magliano MP, Simeone DM. Deciphering the role of stroma in pancreatic cancer. *Curr Opin Gastroenterol* 2013;29:537–43.
3. Ohlund D, Elyada E, Tuveson D. Fibroblast heterogeneity in the cancer wound. *J Exp Med* 2014;211:1503–23.
4. Veenstra VL, Garcia-Garito A, van Laarhoven HW, Bijlsma MF. Extracellular influences: molecular subclasses and the microenvironment in pancreatic cancer. *Cancers (Basel)* 2018;10(2):pii: E34. doi: 10.3390/cancers10020034.
5. Bolm L, Cigolla S, Wittel UA, Hopt UT, Keck T, Rades D, et al. The Role of fibroblasts in pancreatic cancer: extracellular matrix versus paracrine factors. *Transl Oncol* 2017;10:578–88.

6. Olive KP, Jacobetz MA, Davidson CJ, Gopinathan A, McIntyre D, Honess D, et al. Inhibition of Hedgehog signaling enhances delivery of chemotherapy in a mouse model of pancreatic cancer. *Science* 2009;324:1457–61.
7. Provenzano PP, Cuevas C, Chang AE, Goel VK, Von Hoff DD, Hingorani SR. Enzymatic targeting of the stroma ablates physical barriers to treatment of pancreatic ductal adenocarcinoma. *Cancer Cell* 2012;21:418–29.
8. Jacobetz MA, Chan DS, Nemesse A, Bapiro TE, Cook N, Frese KK, et al. Hyaluronan impairs vascular function and drug delivery in a mouse model of pancreatic cancer. *Gut* 2013;62:112–20.
9. Rice AJ, Cortes E, Lachowski D, Cheung BCH, Karim SA, Morton JP, et al. Matrix stiffness induces epithelial-mesenchymal transition and promotes chemoresistance in pancreatic cancer cells. *Oncogenesis* 2017;6:e352.
10. Laklai H, Miroshnikova YA, Pickup MW, Collisson EA, Kim GE, Barrett AS, et al. Genotype tunes pancreatic ductal adenocarcinoma tissue tension to induce matricellular fibrosis and tumor progression. *Nat Med* 2016;22:497–505.
11. Olivares O, Mayers JR, Gouirand V, Torrence ME, Gicquel T, Borge L, et al. Collagen-derived proline promotes pancreatic ductal adenocarcinoma cell survival under nutrient limited conditions. *Nat Commun* 2017;8:16031.
12. Dima SO, Tanase C, Albulescu R, Herlea V, Chivu-Economescu M, Purnichescu-Purtan R, et al. An exploratory study of inflammatory cytokines as prognostic biomarkers in patients with ductal pancreatic adenocarcinoma. *Pancreas* 2012;41:1001–7.
13. Tjomsland V, Niklasson L, Sandstrom P, Borch K, Druid H, Bratthall C, et al. The desmoplastic stroma plays an essential role in the accumulation and modulation of infiltrated immune cells in pancreatic adenocarcinoma. *Clin Dev Immunol* 2011;2011:212810.
14. Erez N, Truitt M, Olson P, Arron ST, Hanahan D. Cancer-associated fibroblasts are activated in incipient neoplasia to orchestrate tumor-promoting inflammation in an NF-kappaB-dependent manner. *Cancer Cell* 2010;17:135–47.
15. Sherman MH, Yu RT, Engle DD, Ding N, Atkins AR, Tiriach H, et al. Vitamin D receptor-mediated stromal reprogramming suppresses pancreatitis and enhances pancreatic cancer therapy. *Cell* 2014;159:80–93.
16. Ohlund D, Handly-Santana A, Biffi G, Elyada E, Almeida AS, Ponz-Sarvise M, et al. Distinct populations of inflammatory fibroblasts and myofibroblasts in pancreatic cancer. *J Exp Med* 2017;214:579–96.
17. Feig C, Jones JO, Kraman M, Wells RJ, Deonaraine A, Chan DS, et al. Targeting CXCL12 from FAP-expressing carcinoma-associated fibroblasts synergizes with anti-PD-L1 immunotherapy in pancreatic cancer. *Proc Natl Acad Sci U S A* 2013;110:20212–7.
18. Zhang Y, Yan W, Collins MA, Bednar F, Rakshit S, Zetter BR, et al. Interleukin-6 is required for pancreatic cancer progression by promoting MAPK signaling activation and oxidative stress resistance. *Cancer Res* 2013;73:6359–74.
19. Ozdemir BC, Pentcheva-Hoang T, Carstens JL, Zheng X, Wu CC, Simpson TR, et al. Depletion of carcinoma-associated fibroblasts and fibrosis induces immunosuppression and accelerates pancreas cancer with reduced survival. *Cancer Cell* 2014;25:719–34.
20. Rhim AD, Oberstein PE, Thomas DH, Mirek ET, Palermo CF, Sastra SA, et al. Stromal elements act to restrain, rather than support, pancreatic ductal adenocarcinoma. *Cancer Cell* 2014;25:735–47.
21. Lee JJ, Perera RM, Wang H, Wu DC, Liu XS, Han S, et al. Stromal response to Hedgehog signaling restrains pancreatic cancer progression. *Proc Natl Acad Sci U S A* 2014;111:E3091–100.
22. Kim EJ, Sahai V, Abel EV, Griffith KA, Greenon JK, Takebe N, et al. Pilot clinical trial of hedgehog pathway inhibitor GDC-0449 (vismodegib) in combination with gemcitabine in patients with metastatic pancreatic adenocarcinoma. *Clin Cancer Res* 2014;20:5937–45.
23. Catenacci DV, Junttila MR, Karrison T, Bahary N, Horiba MN, Nattam SR, et al. Randomized phase Ib/II study of gemcitabine plus placebo or vismodegib, a hedgehog pathway inhibitor, in patients with metastatic pancreatic cancer. *J Clin Oncol* 2015;33:4284–92.
24. Zheng GX, Terry JM, Belgrader P, Ryvkin P, Bent ZW, Wilson R, et al. Massively parallel digital transcriptional profiling of single cells. *Nat Commun* 2017;8:14049.
25. Macosko EZ, Basu A, Satija R, Nemesh J, Shekhar K, Goldman M, et al. Highly parallel genome-wide expression profiling of individual cells using nanoliter droplets. *Cell* 2015;161:1202–14.
26. Moffitt RA, Marayati R, Flate EL, Volmar KE, Loeza SG, Hoadley KA, et al. Virtual microdissection identifies distinct tumor- and stroma-specific subtypes of pancreatic ductal adenocarcinoma. *Nat Genet* 2015;47:1168–78.
27. Bailey P, Chang DK, Nones K, Johns AL, Patch AM, Gingras MC, et al. Genomic analyses identify molecular subtypes of pancreatic cancer. *Nature* 2016;531:47–52.
28. Collisson EA, Sadanandam A, Olson P, Gibb WJ, Truitt M, Gu S, et al. Subtypes of pancreatic ductal adenocarcinoma and their differing responses to therapy. *Nat Med* 2011;17:500–3.
29. MacParland SA, Liu JC, Ma XZ, Innes BT, Bartczak AM, Gage BK, et al. Single cell RNA sequencing of human liver reveals distinct intra-hepatic macrophage populations. *Nat Commun* 2018;9:4383.
30. Georgoudaki AM, Prokopec KE, Boura VF, Hellqvist E, Sohn S, Ostling J, et al. Reprogramming tumor-associated macrophages by antibody targeting inhibits cancer progression and metastasis. *Cell Rep* 2016;15:2000–11.
31. Schuch K, Wanko B, Ambroz K, Castelo-Rosa A, Moreno-Viedma V, Grun NG, et al. Osteopontin affects macrophage polarization promoting endocytic but not inflammatory properties. *Obesity (Silver Spring)* 2016;24:1489–98.
32. Zhang Y, Du W, Chen Z, Xiang C. Upregulation of PD-L1 by SPP1 mediates macrophage polarization and facilitates immune escape in lung adenocarcinoma. *Exp Cell Res* 2017;359:449–57.
33. Hildner K, Edelson BT, Purtha WE, Diamond M, Matsushita H, Kohyama M, et al. Batf3 deficiency reveals a critical role for CD8alpha+ dendritic cells in cytotoxic T cell immunity. *Science* 2008;322:1097–100.
34. Spranger S, Dai D, Horton B, Gajewski TF. Tumor-residing Batf3 dendritic cells are required for effector T cell trafficking and adoptive T cell therapy. *Cancer Cell* 2017;31:711–23.
35. Schmidt SV, Nino-Castro AC, Schultze JL. Regulatory dendritic cells: there is more than just immune activation. *Front Immunol* 2012;3:274.
36. Shurin GV, Ma Y, Shurin MR. Immunosuppressive mechanisms of regulatory dendritic cells in cancer. *Cancer Microenviron* 2013;6:159–67.
37. Munn DH, Sharma MD, Lee JR, Jhaveri KG, Johnson TS, Keskin DB, et al. Potential regulatory function of human dendritic cells expressing indoleamine 2,3-dioxygenase. *Science* 2002;297:1867–70.
38. Zhang Y, Yan W, Mathew E, Bednar F, Wan S, Collins MA, et al. CD4+ T lymphocyte ablation prevents pancreatic carcinogenesis in mice. *Cancer Immunol Res* 2014;2:423–35.
39. Shimizu J, Yamazaki S, Sakaguchi S. Induction of tumor immunity by removing CD25+CD4+ T cells: a common basis between tumor immunity and autoimmunity. *J Immunol* 1999;163:5211–8.
40. Onizuka S, Tawara I, Shimizu J, Sakaguchi S, Fujita T, Nakayama E. Tumor rejection by in vivo administration of anti-CD25 (interleukin-2 receptor alpha) monoclonal antibody. *Cancer Res* 1999;59:3128–33.
41. Tan MC, Goedegebuure PS, Belt BA, Flaherty B, Sankpal N, Gillanders WE, et al. Disruption of CCR5-dependent homing of regulatory T cells inhibits tumor growth in a murine model of pancreatic cancer. *J Immunol* 2009;182:1746–55.
42. Tang Y, Xu X, Guo S, Zhang C, Tang Y, Tian Y, et al. An increased abundance of tumor-infiltrating regulatory T cells is correlated with the progression and prognosis of pancreatic ductal adenocarcinoma. *PLoS One* 2014;9:e91551.
43. Jang JE, Hajdu CH, Liot C, Miller G, Dustin ML, Bar-Sagi D. Crosstalk between regulatory T cells and tumor-associated dendritic cells negates anti-tumor immunity in pancreatic cancer. *Cell Rep* 2017;20:558–71.
44. Li H, Courtois ET, Sengupta D, Tan Y, Chen KH, Goh JLL, et al. Reference component analysis of single-cell transcriptomes elucidates

- cellular heterogeneity in human colorectal tumors. *Nat Genet* 2017; 49:708–18.
45. Hirayama K, Kono H, Nakata Y, Akazawa Y, Wakana H, Fukushima H, et al. Expression of podoplanin in stromal fibroblasts plays a pivotal role in the prognosis of patients with pancreatic cancer. *Surg Today* 2018;48:110–8.
 46. Fadic R, Mezzano V, Alvarez K, Cabrera D, Holmgren J, Brandan E. Increase in decorin and biglycan in duchenne muscular dystrophy: role of fibroblasts as cell source of these proteoglycans in the disease. *J Cell Mol Med* 2006;10:758–69.
 47. Stylianopoulos T, Martin JD, Chauhan VP, Jain SR, Diop-Frimpong B, Bardeesy N, et al. Causes, consequences, and remedies for growth-induced solid stress in murine and human tumors. *Proc Natl Acad Sci U S A* 2012;109:15101–8.
 48. Chauhan VP, Martin JD, Liu H, Lacorre DA, Jain SR, Kozin SV, et al. Angiotensin inhibition enhances drug delivery and potentiates chemotherapy by decompressing tumour blood vessels. *Nat Commun* 2013;4:2516.
 49. Biffi G, Oni TE, Spielman B, Hao Y, Elyada E, Park Y, et al. IL1-induced JAK/STAT signaling is antagonized by TGF-beta to shape CAF heterogeneity in pancreatic ductal adenocarcinoma. *Cancer Discov* 2019;9:282–301.
 50. Alvarez MJ, Shen Y, Giorgi FM, Lachmann A, Ding BB, Ye BH, et al. Functional characterization of somatic mutations in cancer using network-based inference of protein activity. *Nat Genet* 2016;48: 838–47.
 51. Lachmann A, Giorgi FM, Lopez G, Califano A. ARACNe-AP: gene network reverse engineering through adaptive partitioning inference of mutual information. *Bioinformatics* 2016;32:2233–5.
 52. Onizuka T, Yuasa S, Kusumoto D, Shimoji K, Egashira T, Ohno Y, et al. Wnt2 accelerates cardiac myocyte differentiation from ES-cell derived mesodermal cells via non-canonical pathway. *J Mol Cell Cardiol* 2012;52:650–9.
 53. Vuga LJ, Ben-Yehudah A, Kovkova-Naumovski E, Oriss T, Gibson KF, Feghali-Bostwick C, et al. WNT5A is a regulator of fibroblast proliferation and resistance to apoptosis. *Am J Respir Cell Mol Biol* 2009;41:583–9.
 54. Hingorani SR, Wang L, Multani AS, Combs C, Deramaudt TB, Hruban RH, et al. Trp53R172H and KrasG12D cooperate to promote chromosomal instability and widely metastatic pancreatic ductal adenocarcinoma in mice. *Cancer Cell* 2005;7:469–83.
 55. Beatty GL, Winograd R, Evans RA, Long KB, Luque SL, Lee JW, et al. Exclusion of T cells from pancreatic carcinomas in mice is regulated by Ly6C(low) F4/80(+) extratumoral macrophages. *Gastroenterology* 2015;149:201–10.
 56. McGowan SE, Torday JS. The pulmonary lipofibroblast (lipid interstitial cell) and its contributions to alveolar development. *Annu Rev Physiol* 1997;59:43–62.
 57. Djurec M, Grana O, Lee A, Troule K, Espinet E, Cabras L, et al. Saa3 is a key mediator of the protumorigenic properties of cancer-associated fibroblasts in pancreatic tumors. *Proc Natl Acad Sci U S A* 2018; 115:E1147–E56.
 58. Boj SF, Hwang CI, Baker LA, Chio II, Engle DD, Corbo V, et al. Organoid models of human and mouse ductal pancreatic cancer. *Cell* 2015;160:324–38.
 59. Liou HC, Boothby MR, Finn PW, Davidson R, Nabavi N, Zeleznik-Le NJ, et al. A new member of the leucine zipper class of proteins that binds to the HLA DR alpha promoter. *Science* 1990;247:1581–4.
 60. Yoshida H, Matsui T, Yamamoto A, Okada T, Mori K. XBP1 mRNA is induced by ATF6 and spliced by IRE1 in response to ER stress to produce a highly active transcription factor. *Cell* 2001;107:881–91.
 61. Boes M, Cerny J, Massol R, Op den Brouw M, Kirchhausen T, Chen J, et al. T-cell engagement of dendritic cells rapidly rearranges MHC class II transport. *Nature* 2002;418:983–8.
 62. Barnden MJ, Allison J, Heath WR, Carbone FR. Defective TCR expression in transgenic mice constructed using cDNA-based alpha- and beta-chain genes under the control of heterologous regulatory elements. *Immunol Cell Biol* 1998;76:34–40.
 63. Yang SY, Denning SM, Mizuno S, Dupont B, Haynes BF. A novel activation pathway for mature thymocytes. Costimulation of CD2 (T,p50) and CD28 (T,p44) induces autocrine interleukin 2/interleukin 2 receptor-mediated cell proliferation. *J Exp Med* 1988;168: 1457–68.
 64. Lee JW, Komar CA, Bengsch F, Graham K, Beatty GL. Genetically engineered mouse models of pancreatic cancer: the KPC model (LSL-Kras(G12D/+);LSL-Trp53(R172H/+);Pdx-1-Cre), its variants, and their application in immuno-oncology drug discovery. *Curr Protoc Pharmacol* 2016;73:14.39.1–14.39.20.
 65. Gopinathan A, Morton JP, Jodrell DI, Sansom OJ. GEMMs as pre-clinical models for testing pancreatic cancer therapies. *Dis Model Mech* 2015;8:1185–200.
 66. Li J, Klughammer J, Farlik M, Penz T, Spittler A, Barbieux C, et al. Single-cell transcriptomes reveal characteristic features of human pancreatic islet cell types. *EMBO Rep* 2016;17:178–87.
 67. Baron M, Veres A, Wolock SL, Faust AL, Gaujoux R, Vetere A, et al. A single-cell transcriptomic map of the human and mouse pancreas reveals inter- and intra-cell population structure. *Cell Syst* 2016; 3:346–60.
 68. Muraro MJ, Dharmadhikari G, Grun D, Groen N, Dielen T, Jansen E, et al. A single-cell transcriptome atlas of the human pancreas. *Cell Syst* 2016;3:385–94.
 69. Wang YJ, Schug J, Won KJ, Liu C, Naji A, Avrahami D, et al. Single-cell transcriptomics of the human endocrine pancreas. *Diabetes* 2016;65:3028–38.
 70. Segerstolpe A, Palasantza A, Eliasson P, Andersson EM, Andreasson AC, Sun X, et al. Single-cell transcriptome profiling of human pancreatic islets in health and type 2 diabetes. *Cell Metab* 2016;24:593–607.
 71. Lawlor N, George J, Bolisetty M, Kursawe R, Sun L, Sivakamasundari V, et al. Single-cell transcriptomes identify human islet cell signatures and reveal cell-type-specific expression changes in type 2 diabetes. *Genome Res* 2017;27:208–22.
 72. Enge M, Arda HE, Mignardi M, Beausang J, Bottino R, Kim SK, et al. Single-cell analysis of human pancreas reveals transcriptional signatures of aging and somatic mutation patterns. *Cell* 2017;171:321–30.
 73. Bernard V, Semaan A, Huang J, San Lucas FA, Mulu FC, Stephens BM, et al. Single cell transcriptomics of pancreatic cancer precursors demonstrates epithelial and microenvironmental heterogeneity as an early event in neoplastic progression. *Clin Cancer Res* 2018;25: 2194–205.
 74. Hosein AN, Huang H, Wang Z, Parmar K, Du W, Huang J, et al. Cellular heterogeneity during mouse pancreatic ductal adenocarcinoma progression at single-cell resolution. *bioRxiv* 2019.
 75. Su S, Chen J, Yao H, Liu J, Yu S, Lao L, et al. CD10(+)GPR77(+) cancer-associated fibroblasts promote cancer formation and chemoresistance by sustaining cancer stemness. *Cell* 2018;172:841–56.
 76. Costa A, Kieffer Y, Scholer-Dahirel A, Pelon F, Bourachot B, Cardon M, et al. Fibroblast Heterogeneity and Immunosuppressive Environment in Human Breast Cancer. *Cancer Cell* 2018;33:463–79.
 77. Lambrechts D, Wauters E, Boeckx B, Aibar S, Nittner D, Burton O, et al. Phenotype molding of stromal cells in the lung tumor microenvironment. *Nat Med* 2018;24:1277–89.
 78. Kumar B, Boucher Y, Liu H, Ferreira D, Hooker J, Catana C, et al. Noninvasive assessment of losartan-induced increase in functional microvasculature and drug delivery in pancreatic ductal adenocarcinoma. *Transl Oncol* 2016;9:431–7.
 79. Dubrot J, Duraes FV, Potin L, Capotosti F, Brighouse D, Suter T, et al. Lymph node stromal cells acquire peptide-MHCII complexes from dendritic cells and induce antigen-specific CD4(+) T cell tolerance. *J Exp Med* 2014;211:1153–66.
 80. Abe J, Shichino S, Ueha S, Hashimoto S, Tomura M, Inagaki Y, et al. Lymph node stromal cells negatively regulate antigen-specific CD4+ T cell responses. *J Immunol* 2014;193:1636–44.
 81. van der Maaten L. Accelerating t-SNE using tree-based algorithms. *J Machine Learn Res* 2014;15:3221–45.
 82. Ester M, Kriegel HP, Sander J, Xu X. A density-based algorithm for discovering clusters in large spatial databases with noise. *Proceedings*

- of the 2nd International Conference on Knowledge Discovery and Data Mining; 1996:226–31.
83. Bolisetty MT, Stitzel ML, Robson P. CellView: interactive exploration of high dimensional single cell RNA-Seq data. *bioRxiv* 2017.
84. Margolin AA, Nemenman I, Basso K, Wiggins C, Stolovitzky G, Dalla Favera R, et al. ARACNE: an algorithm for the reconstruction of gene regulatory networks in a mammalian cellular context. *BMC Bioinformatics* 2006;7:S7.
85. Catena R, Montuenga LM, Bodenmiller B. Ruthenium counterstaining for imaging mass cytometry. *J Pathol* 2018;244:479–84.
86. Subramanian A, Tamayo P, Mootha VK, Mukherjee S, Ebert BL, Gillette MA, et al. Gene set enrichment analysis: a knowledge-based approach for interpreting genome-wide expression profiles. *Proc Natl Acad Sci U S A* 2005;102:15545–50.
87. Robinson MD, McCarthy DJ, Smyth GK. edgeR: a Bioconductor package for differential expression analysis of digital gene expression data. *Bioinformatics* 2010;26:139–40.
88. Trapnell C, Cacchiarelli D, Grimsby J, Pokharel P, Li S, Morse M, et al. The dynamics and regulators of cell fate decisions are revealed by pseudotemporal ordering of single cells. *Nat Biotechnol* 2014;32:381–6.